From passive degassing to violent Strombolian eruption: the case of the 2008 eruption of Llaima volcano, Chile.

Dawn C.S. Ruth[1,2*†], Elizabeth Cottrell[2], Joaquín A. Cortés[3], Katherine A. Kelley[4], Eliza S. Calder[3]

***** Corresponding author: sdawn@ntu.edu.sg

† Now at Earth Observatory of Singapore, Nanyang Technological University, Singapore, 639798

1. Department of Geology, State University of New York at Buffalo, Buffalo, NY 14260, USA
2. Smithsonian Institution, National Museum of Natural History, Washington, DC, 20560, USA
3. School of Geosciences, University of Edinburgh, Scotland, EH9 3JW
4. Graduate School of Oceanography, University of Rhode Island, Narragansett, RI, 02882, USA

ABSTRACT

On 1 January 2008 Llaima volcano, a basaltic andesite stratocone in southern Chile, entered a phase of violent Strombolian eruption. Llaima, like many passively degassing systems, has experienced prolonged (decades-long) periods of persistent summit degassing from its open vent. The rapid transition from long-lived passive degassing to violent explosive eruption occurred with limited precursory monitoring signals. This paper is motivated by the desire to understand what occurs in these systems when that switch takes place. To this end, we study the products of the 2008 violent Strombolian eruption of Llaima volcano, Chile. We present new textural analyses of scoria and geochemical data from five whole rock samples, troctolite glomerocrysts with and without Cr-spinel, and 182 olivine-hosted melt inclusions from tephra samples. Two populations of scoria ("brown" and "black") are distinguished by variable crystallinity and vesicularity, but are geochemically indistinguishable. Black scoria contain abundant microlites with tabular to acicular morphologies and convolute vesicles up to 1.75 mm in effective diameter. The brown scoria tend to have fewer, acicular microlites, abundant matrix glass, and round vesicles with a narrower size distribution constrained to <0.4 mm in diameter. Overall, textures from the black and brown scoria evidence a textural maturation process where shallow system magma becomes more crystal rich and likely rheologically stiffer as a result of prolonged passive degassing. The Cr-spinel and Cr-spinel free troctolite glomerocrysts have plagioclase and olivine compositions of An_{65-92} and Fo_{81}, respectively. Cr# in the Cr-spinel range from 26-37; these are consistent with magma originating from the deeper plumbing system. Whole rock compositions for the tephra average 51 wt% SiO_2, 18 wt% Al_2O_3, and ~6 wt% MgO. The major elements of olivine-hosted melt inclusions range from 49 to 56 wt% SiO_2, and 3.72 to 7.76 wt% MgO; there was no distinct compositional difference between olivine-hosted melt

inclusions sourced from the different scoria. Melt inclusion volatile contents range from below detection up to 2.95 wt% H_2O, and 1973 ppm CO_2 (though not in the same melt inclusion). H_2O and CO_2 concentrations are consistent with open system degassing and, when compared with fractionation indices (e.g. K_2O), indicate coupled degassing and crystallization throughout the system. The majority of melt inclusions denote a single liquid line of descent indicative of plagioclase and olivine fractionation. Entrapment pressures range from 8-342 MPa and fall into two groups: 8-100 MPa (300 m to ~4 km depth) and > 100 MPa (4-14 km), revealing that this eruption tapped a deep plumbing system.

We propose here that passive degassing at Llaima is maintained by periodic small-batch magma injections. Consequently, due to extensive degassing the upper plumbing system magma crystallized and increased in viscosity. Before the 2008 eruption, some volatiles sourced from the repeatedly-injected magmas, exsolved from the inferred crystal mush, and ascending from deeply-sourced degassing magmas gradually accumulated within the crystal mush and beneath the stiffened conduit magma. Our results support a model where eruption triggering occurred when magma injection remobilized the mush and, importantly, unlocked the accumulated gasses that ascended rapidly, and generated the observed violent Strombolian explosive activity. Our proposed model contrasts with those models for explosive mafic volcanism which require rapid magma ascent under closed system degassing conditions. Importantly, our proposed mechanism provides a means for systems with dominantly open system degassing behavior to transition from passive degassing to explosive eruptions.

Keywords: Basaltic andesite; eruption trigger; magma recharge; melt inclusions; open vent volcanism; passive degassing; regulated gas transport

INTRODUCTION

On the 1st of January 2008, Llaima volcano in the Southern Andean Volcanic Zone, Chile, entered a new phase of intense explosive activity. The eruption, described as a violent Strombolian type eruption, was characterized by highly pulsatory fire fountaining and the development of a 10 km high ash plume (Ruth and Calder, 2014). Prior to the eruption the volcano exhibited persistent passive degassing at least since its previous eruption in 1994 (OVDAS, 2008). Passive degassing (sometimes called persistent degassing, or quiescent degassing) is characterized by volatile outgassing, usually from a summit vent, but is commonly associated with limited or negligible magma net flux out of the system. In many cases volcanoes exhibiting this behavior are typified by mafic magmas and open vents, and the persistent degassing can continue for months to years (Rosi et al., 2000; Rose et al., 2013). In contrast, violent Strombolian eruptions (often referred to as paroxysms, or cineritic eruptions) are characterized by moderately-sized, sustained ash plumes (> 10 km in altitude) and dispersed tephra deposits (Francis et al 1990; Valentine and Gregg, 2008; Houghton and Gonnermann, 2008). Violent Strombolian eruptions are known to occur periodically at volcanoes that commonly present passive degassing, including, Stromboli, Italy (Barberi et al., 1993; Rosi et al., 2000; Rosi et al., 2013); Llaima and Villarrica, in Chile (Petit-Breuihl, 2006; OVDAS, 2008), Masaya, Nicaragua (Williams, 1983); and Fuego, Guatemala (Rose et al., 2008). Where these violent explosive eruptions occur from open, already passively degassing systems, their onset can be sudden, sometimes with little to no advance warning or signals in monitoring data. The hazards associated with such events (ballistics, tephra fall, lava flows, and sometimes lahars) can be challenging to ameliorate due to the sudden onset nature, especially if the volcano is located in a region of high population (e.g. Rose et al., 2008; Rose et al., 2013; Rosi et al., 2013).

87 Understanding the mechanisms that initiate this rapid change in behavior, from passive
88 degassing to violent explosive activity, is therefore a key challenge to improving our capacity to
89 deal with explosive basaltic volcanism.

90 Investigations on this style of explosive basaltic volcanism have been undertaken at
91 Stromboli, Mt. Etna, Parícutin, and Cerro Negro (Allard, 1997; Roggensack et al., 1997; Métrich
92 et al., 2001; Lautze and Houghton, 2007; Pioli et al., 2008; Johnson et al., 2010; Métrich et al.,
93 2010). Violent Strombolian eruptions necessitate not only high mass fluxes of magma (e.g., mass
94 eruption rates 10^3-10^5 kg s^{-1}), but also, critically, high instantaneous gas fluxes (Pioli et al., 2009;
95 2009). In several eruption cases, the triggering of these events have been attributed to bouts of
96 recharge of mafic magma that ascend rapidly through the system, e.g. Stromboli (Métrich et al.,
97 2001; Bertagnini et al, 2003; Métrich et al., 2010), Parícutin (Lurh, 2001; Pioli et al., 2008), and
98 Cerro Negro (Roggensack et al., 1997). Deeply-sourced magma injection into a relatively
99 shallow reservoir is inferred from the volatile contents of mineral-hosted melt inclusions. The
100 inferred rapid closed system ascent and subsequent degassing of H_2O in these magmas then drive
101 the sporadic explosive eruptions, often producing texturally bimodal scoria populations with
102 chemically distinct olivine hosted melt inclusions (e.g., Métrich et al., 2010). However this
103 model does not work for systems where erupted products record dominantly open system
104 degassing behavior (e.g. Anak Krakatau, Mandeville et al., 1998), or systems that are not well
105 characterized by either closed or open system degassing (e.g. Johnson et al., 2010; Oppenheimer
106 et al., 2011). Alternative mechanisms that have been proposed to explain the transition from
107 passive degassing or low intensity eruptions to violent explosive eruptions include changes in
108 magma system geometry (Palma et al., 2011; Genereau et al., 2010) and changes in the fluid
109 dynamics during magma ascent (Jaupart, 1998; Houghton and Gonnermann, 2008).

Studies of the products of the 2008 eruption of Llaima have been undertaken by Bouvet de Maisonneuve et al. (2012a, 2012b) and Ruth and Calder (2014). Ruth and Calder (2014) report on morphological, textural and dispersal characteristics of the diverse tephra types, including distinctive plate tephra. Bouvet de Maisonneuve et al. (2012a) present olivine hosted melt inclusion data for the 2008 scoria, as well as for three historical eruptions in 1957, and ~1850 AD (separated into upper and lower tephras). Their melt inclusion dataset evidences a persistent shallow plumbing system (< ~130 MPa) through this time, but provides limited evidence for consistent degassing and fractionation trends. For the 2008 eruption, mineral zoning and chemistry data suggest repeated pre-eruption magma injection (Bouvet de Maisonneuve et al., 2012b). Based on these findings, they propose that the 2008 eruption was triggered by remobilization of a crystal mush (i.e. magmatic regions with >50% crystals) by magma recharge. The Bouvet de Maisonneuve et al. (2012a, 2012b) work provides an excellent framework for understanding reservoir processes associated with several of the recent major eruptive episodes at Llaima, but key aspects of the 2008 eruption remain unaccounted for.

In this work we focus specifically on the products of the 2008 eruption. We extend the work undertaken by both Bouvet de Maisonneuve et al., (2012a, 2012b) and Ruth and Calder (2014) and use a combined textural and geochemical analysis that both complements previous work, and provides new information about the shallow and deeper system. Specifically, we build on the previous work in the follow ways: 1) Ruth and Calder (2014) identified texturally heterogeneous tephra produced during the violent explosive phase of the 2008 eruption. Here we use textural data, including vesicle and crystal size distributions, from these different tephra to investigate crystallization and degassing processes in the shallow system and discuss these in the context of the explosive eruptive activity. This information is important because shallow

degassing and crystallization are considered critical processes that can lead to increases in the intensity of mafic eruptions (e.g. Sable et al., 2006; Houghton and Gonnermann, 2008). 2) From the different tephra types we provide major, trace, and volatile elements from 182 olivine-hosted melt inclusions, thereby extending the work of Bouvet de Maisonneuve et al. (2012a, 2012b). Our comprehensive geochemical data show evidence of a deeper, more CO_2-rich plumbing system than previously reported. 3) We consider it important that any conceptual model for the Llaima plumbing system places the 2008 eruptive episode in the context of the persistently active passive degassing system, which typified the activity both before that eruption occurred and afterwards. Although Bouvet de Maisonneuve et al. (2012a, 2012b) focused dominantly on the nature of the magmatic plumbing and crystal mush processes, the role of gas accumulation was not investigated. Here, bearing in mind that high gas fluxes resulting in highly pulsatory lava fountaining is a key driver of violent Strombolian eruptions (e.g. Pioli et al., 2009), we discuss potential scenarios for gas accumulation within the Llaima plumbing system. Finally we propose a model for the transition in activity style from passive degassing to violent explosive eruptions.

LLAIMA VOLCANO AND THE 1 JANUARY 2008 ERUPTION

Llaima volcano (38°41′45″S 71°43′54″W, 3179 m a.s.l) is a basaltic andesite stratocone located in the Southern Volcanic Zone (SVZ) of the Chilean Andes about ~600 km south of Santiago (Fig. 1). Llaima is one of the most historically active volcanoes in the SVZ with 54 eruptions since 1640 (Naranjo and Moreno, 2005; Petit-Breuihl, 2006). Statistical analysis of the historic record for eruptions of VEI $\geq$ 2 indicates an eruption recurrence interval of ~6 years (Dzierma and Wehrmann, 2010). Major explosive activity producing significant eruption plumes (>10 km) and associated tephra deposits occurred most recently in 1957 (Hantke, 1962; Naranjo

and Moreno, 2005), with a similar, but lower intensity eruption occurring in May 1994 (Moreno and Fuentealba, 1994). The 1994 eruption lasted 8 hours, produced lava fountains, a 7 km altitude plume and associated tephra deposit, and lahars down the western flanks; the eruption was characterized at VEI 2 (Moreno and Fuentealba, 1994).

On 1 January 2008, between 1730 and 1820 local time (GMT - 04:00), a summit eruption began at Llaima. The eruption was characterized by violent pulsating Strombolian and fire fountaining activity which produced a plume reaching ~11 km high. Lava flows were generated on the west flank, and lahars were generated in the Rio Calbuco and Rio Captrén valleys, respectively (Global Volcanism Program, 2008) and resulted in the evacuation of the Conguillío National Park. The main explosive phase lasted ~13 hours, but eruptive activity continued with reduced but intermittent Strombolian activity continuing through July 2008. A second explosive phase occurred on 3 April 2009; and the extended eruptive phase ended by July 2009. In all, the 2008-2009 eruptive phase produced lava flows extending 3 km from the vent onto the western and southern flanks, a tephra deposit with a minimum eruption volume of 1.3×10^6 kg m^{-3} (Ruth and Calder, 2014), pyroclastic flow deposits over snow (i.e. mixed avalanches) associated with an observed vent on the (north) eastern flank, and lahars formed from the interaction of lava and summit glacier. Retrospectively, minor increases in seismic activity and minor ash explosions were recognized in May and June 2007 but otherwise there was little/no precursory activity (OVDAS, pers. comm.). There is also no evidence that significant edifice deformation occurred prior to January 2008 (Fournier et al., 2010; Remy et al., 2015; Delgado et al., submitted).

SAMPLE COLLECTION AND PREPARATION

The tephra samples studied here are from the initial phase of the 2008 eruption, collected in January 2009 and January 2011 from a total of 94 different sites in the fall deposit on the eastern flanks of the volcano (Ruth and Calder, 2014). The tephra samples were characterized in the field based on hand sample color, texture, and morphology as either black scoria, brown scoria, or plate tephra. The black scoria and plate tephra only differ in shape, and can otherwise be considered similar (Ruth and Calder, 2014). From these, twenty thin sections of representative tephra types were made for textural analysis using conventional petrography and back-scattered electron (BSE) imaging. BSE images were collected using the Hitachi SU-70 scanning electron microscope at the University at Buffalo South Campus Instrument Center (SCIC) and the FEI Nova NanoSEM 600 in the Department of Mineral Sciences at the National Museum of Natural History (NMNH), Smithsonian Institution.

Tephra were separated by type (black and brown scoria, and plate tephra) and were lightly crushed using a jaw crusher and shaker sieved with screen sizes of 25, 40, and 80 mesh (e.g., openings of 710, 425, and 180 μm, respectively). Whole rock analyses were conducted on the > 25 mesh separate, as well as gravel-sized hand-picked samples where homogeneity could be ensured. Olivine phenocrysts were hand-picked from the 25 and 40 mesh separates of the crushed tephra.

Clear, naturally quenched, glassy melt inclusions hosted in olivine crystals were selected for analysis (see supplemental material for database of melt inclusions) (Fig. 2). Melt inclusions containing daughter crystals were excluded. Some melt inclusions showed visible fractures but the fractures did not extend to the crystal surface. Melt inclusions contained zero to one vapor bubble. We include in the supplemental data the approximate location in the host olivine of the

melt inclusions. Acceptable samples were mounted in epoxy in single-grain mounts to create wafered samples with the inclusions double-side exposed and polished. A total of 182 melt inclusions were analyzed.

ANALYTICAL METHODS

X-ray Fluorescence

Whole rock major elements and some trace elements (Rb, Sr, Y, Zr, V, Ni, Cr, Nb, Ga, Cu, Zn, Co, Ba, La, Ce, U, Th, Sc, Pb) for five tephra samples were analyzed with a PANanalytical 2404 X-ray fluorescence spectrometer (XRF) hosted at Franklin and Marshall College, Pennsylvania. Major element analyses were conducted on dried powder mixed with lithium tetraborate. The mixture was melted in a platinum crucible and then quenched into a flat, glass disk. Total iron as Fe_2O_3 was reported from the XRF analysis and the speciation of iron was measured using titration on a separate aliquot from the crushed samples (after Reichen and Fahey, 1962). Loss on ignition was determined after samples were heated for one hour at 950 °C. The whole-rock powder was mixed with a high purity Copolywax powder and then pressed into a briquette. Trace elements analyses were conducted on this briquette. Calibration curves were constructed with standards listed in Abbey (1983) and Govindaraju (1994). One sample was run in triplicate to determine reproducibility. For SiO_2, Al_2O_3, CaO, Na_2O the replicate analyses showed a < 1% difference; Fe_2O_3, TiO_2, MgO, and K_2O had a 1-2% difference. Replicate P_2O_5 and MnO analyses were identical.

Electron Microprobe

Major element analyses of carbon-coated melt inclusions, matrix glass, plagioclase, and olivine were collected using the five-spectrometer JEOL 8900 electron microprobe (EMPA) located at The National Museum of Natural History, Smithsonian Institution. Select plagioclase and matrix glass analyses were obtained with the JEOL 8900 electron microprobe at Cornell University. Spinel inclusions in the glomerocrysts were analyzed using the five-spectrometer JEOL JXA-8430 field emission electron microprobe located at the Facilities for Analysis, Classification and Testing (FACTS) at Nanyang Technological University, Singapore. Glass analyses were collected on at least five spots per melt inclusion with a 10 μm beam diameter, 15 keV accelerating voltage, and 10 nA beam current (see supplemental materials for details). To minimize alkali loss, we analyze Na and K first, and for shorter on peak durations (10 sec). Our chosen wide beam diameter also minimizes alkali loss (e.g. Hayward, 2011). These techniques are reasonable since analysis of standards as unknowns (e.g. VG-2) returns Na_2O totals within 3% of reported values. Sulfur and chlorine were run after the major element analysis on a minimum of three new spots with 15 keV, 80 nA beam current, and 10 μm beam diameter. Sulfur peaks were initially obtained via a peak search routine on individual melt inclusions. Since the peak position did not shift more than 2%, the peak position was determined using the search routine on scapolite during standardization. The closest (~5-10 μm from the melt inclusion) olivine probe point to the melt inclusion was considered the host olivine composition. Olivine analyses were collected with 15 keV, 40 nA beam current, and 1 μm beam diameter. Plagioclase (in thin section and the glomerocrysts) analyses were obtained with an accelerating voltage of 15 keV, 15 nA beam current, and 5 μm beam diameter. Beam conditions for the spinel analyses were: 15 keV, 20 nA, and 1 μm beam diameter. For all analyses, backgrounds on each side of the peak were counted each for half the peak count times. Beam drift was assessed by

running standards (glass: VG-2; plagioclase: Bytownite; olivine: San Carlos olivine) as an unknown throughout the analytical run and calculating the percent deviation from reported values.

Fourier Transform Infrared Spectroscopy

H_2O and CO_2 concentrations were determined by transmission Fourier Transform Infrared spectroscopy (FTIR) on 49 of the 182 melt inclusions using the Bio-Rad Excalibur spectrometer or the Nicolet 6700 Analytical FTIR hosted at The National Museum of Natural History, Smithsonian Institution, following the methods of Luhr (2001). To minimize atmospheric interference on the spectra, the system (bench, microscope, and samples) was continually purged with dry, CO_2-free air. The spectral region of interest, 1000-6000 cm^{-1}, was obtained with a liquid nitrogen-cooled MCT detector, KBr beam splitter, and tungsten halogen source. Aperture size was selected to ideally obtain three independent spectra per melt inclusion; they ranged from 11x22 μm to 44x44 μm. For smaller melt inclusions, the spectra measurements overlapped. Thickness data were collected either with a piezometric micrometer, and/or indirectly with the wavelength of fringes from 2000-2700 cm^{-1} (Nichols and Wysoczanski, 2007).

Water concentrations in the melt inclusions were calculated using the total H_2O peak at 3535 cm^{-1} (Stolper, 1982a, 1982b). Dissolved CO_3^{2-} concentrations were quantified using the asymmetric stretch doublet between 1515 cm^{-1} and 1435 cm^{-1} (Dixon et al., 1995). The background-corrected peak intensities were obtained through an Excel fitting routine which builds an optimized, synthetic signal that accounts for the vertical offset, the 1630 cm^{-1} total water peak, the CO_3^{2-} doublet, and a straight line (Newman et al., 2000).

When fringe amplitude prevented a straightforward assessment of the intensity of the carbonate doublet, we calculated the CO_2 content of the fringe-filtered signal. The amplitude and wavelength of the fringes were modeled for each spectrum between 1800 and 2000 cm^{-1} using the curve fitting module in MATLAB (see supplemental material for the MATLAB script). The user imports the FTIR absorbance and wavenumber data via a Microsoft Excel file and selects a region where the script will determine the fringes signal. The fringes signal between 1800 and 2000 cm^{-1} can be modelled simply as a linear function overprinted by a sine function. Note that this region may be overprinted by the Si-O signal from analyzed olivine (Nichols and Wysoczanski, 2007); if overprinting is present then this technique is not suitable to correct for fringes. The script fits a sine curve to the fringes, subtracts this from the original spectrum, and outputs the results into a comma-separated text file. CO_2 values were then re-calculated for the fringe-subtracted signal using the Excel fitting routine described above. The difference between the fringe-filtered and unfiltered calculation is less than 5% (Fig. 3), indicating that the presence of fringes does not significantly affect the quantification of carbonate in these samples. In some cases, the CO_3^{2-} doublet was completely overwhelmed by the fringes and CO_2 values could not be reliably retrieved. The CO_2 detection limit for these melt inclusions (up to 80 μm thick) was ~ 400 ppm. For these samples, we only report H_2O values. In total, we performed this correction on spectra from 12 melt inclusions (see supplemental material for raw and fringe-corrected data).

Water was quantified using the spline function built-in in the Thermo Fischer OMNIC spectral analysis software package. Peak heights were collected on the background corrected spectra. Molar absorptivities at 1515 and 1435 cm^{-1} for C and 1635, 4500, and 5200 cm^{-1} for H species were corrected for major element composition according to Dixon et al. (1995). A

constant value for molar absorptivity of 63 mol^{-1} cm^{-1} was applied to all 3535 cm^{-1} peaks as it is not sensitive to composition (Dixon et al., 1995; Kelley and Cottrell, 2012).

Secondary Ion Mass Spectrometry

Secondary ion mass spectrometry (SIMS) was performed on 39 additional melt inclusions because the detection limit for CO_2 by SIMS is lower (~20 ppm) relative to FTIR (~50 ppm) (Hervig et al., 2003). Additional volatile analyses (H_2O, CO_2, S, Cl, F) were collected on a subset of olivine-hosted melt inclusions at the Northeast National Ion Microprobe Facility, Woods Hole Oceanographic Institution, using the Cameca IMS 1280 secondary ion mass spectrometer following the analytical procedure of Helo et al. (2011). These samples were polished to 0.5 micron grit (single-side only), mounted in indium and gold coated samples were then placed under vacuum ($<5x10^{-9}$ torr) and bombarded with a 15 μm, 1.2-1.5 nA, 10kV Cs^+ ion beam to produce the secondary ions (^{12}C, $^{16}O^1H$, ^{19}F, ^{30}Si, ^{32}S, and ^{35}Cl) with ^{30}Si as the reference mass. The samples were pre-sputtered for 4 minutes and the primary beam rastered over an area of 30 x 30 μm. Analysis continued after pre-sputtering with an aperture reduced to 15 x 15 μm. Count times for $^{16}O^1H$ and ^{12}C were 10 s for 10 cycles for a total of 100 s. ^{19}F, ^{30}Si, ^{32}S, and ^{35}Cl count times were 5 s for 10 cycles for a total of 50 s. Calibration curves for measured $^{12}C/^{30}Si$, $^{16}O^1H/^{30}Si$, $^{19}F/^{30}Si$, $^{32}S/^{30}Si$, $^{35}Cl/^{30}Si$ versus the respective volatile concentration were built from the analysis of 11 standard basaltic to andesite glasses (49-57 wt% SiO_2) (Helo et al., 2011) using a York regression (see supplement for calibration curves). R^2 values were 0.99 for all volatiles measured; the reported error includes the measurement error and the error in the linear fit (see supplemental material).

315 **Laser Ablation Inductively Coupled Plasma Mass Spectroscopy**

316 129 melt inclusions were analyzed for thirty-nine trace elements using laser ablation
317 inductively coupled plasma mass spectroscopy (LA-ICPMS). These analyses were done using
318 the Thermo X-Series II quadrupole ICP-MS coupled with a New Wave UP 213 Nd-YAG laser
319 ablation system located at the Graduate School of Oceanography, University of Rhode Island.
320 Spot sizes ranged from 20 – 80 μm depending on melt inclusion size. Ablation time was
321 maximized for the wafered samples with an energy output of 60% and 5 Hz repeat rate.
322 Background and washout were collected for 30 seconds, and the maximum analytical time was
323 60 seconds. Our methodology was modified from Kelley et al. (2003) and Lytle et al. (2012). We
324 used ^{43}Ca as an internal standard and calibrated on eight natural glasses from the USGS (BIR-1g,
325 BHVO-2g, BCR-2g) and Max Planck Institute (GOR132-G, StHls-G, T1-G, ML3B-G, KL2-G);
326 reference values are as reported in Kelley et al. (2003), Jochum et al. (2006), and Lytle et al.
327 (2012). Acceptable linear calibration curves had $R^2 > 0.995$ (see supplemental material for more
328 information). For Ag, Pt, and W, a lower R^2 value is reported due to limited studies on the
329 standards used. Lab reproducibility is ≤ 5% for most trace elements.

330

331 **X-ray Absorption Near Edge Structure Spectroscopy - (micro-XANES)**

332 Two melt inclusions (blk3-2011 and blk1-2010) were analyzed *in situ* for $Fe^{3+}/\sum Fe$ ratios
333 using micro X-ray Absorption Near Edge Structure (micro-XANES) spectroscopy with precision
334 of ±0.005 (Cottrell et al., 2009). Following the methods of Cottrell et al. (2009), the two melt
335 inclusions were analyzed on beamline X26a located at the National Synchrotron Light Source,
336 Brookhaven National Lab. Spectra that included olivine interference were excluded (e.g., Kelley
337 and Cottrell, 2009; Brounce et al., 2014).

TEXTURAL ANALYSIS METHODS AND DEFINITIONS

Definitions

Textural analysis of crystal assemblages provides information about the kinetics of magmatic processes, especially crystallization and degassing (Hammer, 2008). We define phenocrysts here as crystals that are > 100 μm and microphenocrysts as crystals that range from 30 to 100 μm. Microlites are crystals under 30 μm. Vesicles are described as rounded or convolute (i.e. irregular perimeters). Qualitative crystal shape terms used in sample characterization include acicular, tabular, swallow-tail and hopper morphologies (e.g. Lofgren, 1974; Couch et al., 2003; Crabtree and Lange, 2011) (Fig. 4). Acicular crystals are characterized by needle shape habits whereas tabular crystals are rectangular. Swallow-tail plagioclase crystals have forked terminations, often with acicular habits. Hopper (or skeletal) morphology plagioclase crystals are those with voids often in the center (Fig. 4).

Vesicle Size Distributions

We measured the vesicle size distributions (VSDs) to quantify the textural differences between the scoria (e.g. Polacci et al., 2006; Moitra et al., 2013). BSE images at x70 and x90 magnification were made binary for vesicles or crystals. Vesicle walls were manually drawn in the images in the case of breakage during sample preparation. First, we determined the phenocryst areas by manually tracing each crystal in an image; these values were subtracted from the total area measured. Then, where necessary, we reconstructed all bubble walls if portions of the septum were visible to quantify the maximum number of vesicles per image. More than 1000 vesicles were measured per thin section for two black and brown scoria samples, respectively. The vesicle data obtained include: area, major axis, minor axis, and perimeter. Equivalent radius

and diameter were calculated from the area values. Since we are interested in an internal comparison, here we report 2D values to avoid complications due to stereological conversion (Polacci et al., 2006).

Crystal Size Distributions

We used BSE images to collect crystal size data of plagioclase crystals from the brown and black scoria. Long and short axes were measured using ImageJ freeware (http://rsb.info.nih.gov/ij/). We estimated crystal aspect ratios using the CSDSlice technique (Morgan and Jerram, 2006) and considered the textural fabric as massive; we did not correct for crystal roundness. Using petrography and built-in features of ImageJ, we determined the total slide area, volumetric phase abundance, and vesicularity. With these data we calculated the crystal size distributions (CSDs) of the plagioclase using the CSD Corrections 1.51 (http://www.uqac.ca/mhiggins/csdcorrections.html) after Higgins (2006). Higgins (2000) reports maximum errors of ±0.5 ln units in the population density.

PETROGRAPHIC RESULTS

Scoria Textures

The black scoria usually occurs as sub-angular lapilli, although flatter examples (i.e. "plate tephra" - Ruth and Calder, 2014) are common in the proximal (< 9 km) deposit. The brown scoria only occurs as sub-angular, highly vesicular lapilli. General crystallinity (groundmass + phenocrysts) for the black scoria is between 50 to 60 vol%, whereas the brown scoria crystallinity ranges from 10 to 15 vol% (Ruth and Calder, 2014). Average vesicularity for both scoria types was derived from density measurements (after Houghton and Wilson, 1989).

Black scoria vesicles tend to be large, convoluted, with an average vesicularity of 79%. Conversely, vesicles in the brown scoria tend to be smaller and rounder, with an average vesicularity of 88% (Ruth and Calder, 2014).

Phenocryst phase assemblage is plagioclase (~1-2 vol% in brown scoria, 4-7 vol% in black scoria), olivine (<1 vol% in both scoria), rare titanomagnetite and orthopyroxene (<< 1 vol%). Plagioclase is the dominant mineral in the groundmass and is found in all scoria types. Titanomagnetite and orthopyroxene are present as groundmass phases in the black scoria, but are rarely observed in the brown scoria.

Plagioclase phenocrysts show significant signs of disequilibrium including sieve textures and compositional zoning (also observed by Bouvet de Maisonneuve et al., 2012b). Some plagioclase phenocrysts show additional features such as dendrite-like or swallow-tail terminations (Fig. 5a). Plagioclase microphenocrysts have an euhedral, tabular crystal habit and instances of hollow cores, hopper shapes, and minor swallow-tail terminations. They show little to no sieve textures and are sometimes normally zoned; these are found only in the black scoria.

A wide range of microlite morphologies are observed in the black scoria, where habits range from tabular to acicular, often in an interlocking-like configuration (Fig. 5b). Within the brown scoria, microlite habits are dominantly acicular, though tabular microlite are sometimes observed. Crystal free matrix glass is limited within the black scoria, whereas it is more abundant in the brown scoria (Fig. 5c). Additionally, microlite-rich textural domains, similar to the black scoria, are present in the brown scoria (Fig. 5d). Late-stage oxide microlites exhibiting cruciform habits are often found along the boundary separating the two textural domains (Ruth and Calder, 2014). Additional images are provided in the supplemental material. A summary of the textural features of the brown and black scoria is given in Table 1.

Plagioclase and olivine (i.e. troctolite) glomerocryst clusters are also present in all tephra. They are subdivided into two groups based on textural features and mineralogy (Fig. 6). One suite of glomerocrysts shows anhedral, equigranular, plagioclase and olivine with limited amounts of matrix glass containing round vesicles (Fig. 6a). The plagioclase phenocrysts are minimally sieve-textured. Subhedral to euhedral spinel are observed as inclusions in pristine plagioclase and olivine crystals; these are hereafter referred to as Cr-spinel troctolite glomerocrysts. In the other suite of glomerocrysts, the plagioclase phenocrysts show significant sieve textures, the olivine phenocrysts are much smaller and less abundant, matrix glass is generally more abundant with convolute and round vesicles, and the spinel phase is rare (Fig. 6b). These are referred to as Cr-spinel-free troctolite glomerocrysts. Cr-spinel troctolite glomerocrysts are generally found in the brown scoria, whereas the Cr-spinel-free troctolite glomerocrysts are found in the brown and black scoria. The glomerocrysts were noted but not studied by Bouvet de Maisonneuve et al. (2012a), and were thought to originate from a crystal mush. This inference is reasonable given that the glomerocrysts mineral chemistry is similar to that of the scoria. Additionally, it is unlikely that they are assimilated country rock given that the underlying basement comprises evolved Tertiary intrusives (Lucassen et al., 2004).

Crystal and Vesicle Size Distributions

Results from the vesicle textural analysis are shown in Table 2. Vesicle number densities are similar for the brown scoria samples (e.g. 124 and 142), whereas the black scoria samples exhibit higher and lower values (e.g. 106 and 166). The larger vesicle number density value for 1Black is puzzling given that the crystallinity and vesicularity are distinctly different than the brown scoria (see below). One explanation is that the textures could reflect mingling of magma

at different textural stages (e.g. Lautze and Houghton, 2007). The black scoria have a larger average vesicle diameter (0.074 mm) and a wider range of vesicle sizes (<0.01 to 1.74 mm), whereas vesicles in the brown scoria are smaller (0.044-0.055 mm) and are characterized by narrower range of sizes (<0.01 to 0.4 mm) (Fig. 7). The black and brown scoria have broadly similar vesicle size distributions (VSDs) with linear segments (Fig. 7), indicative of steady state nucleation and growth (Mangan and Cashman, 1996). However, the VSD of the black scoria diverges from the brown scoria around 0.1 mm (see Fig. 7 inset), and is characterized by a lower slope indicative of longer growth rates. The brown scoria shows a small plateau in the smallest vesicle diameters, which may reflect the initial stages of vesicle ripening (Mangan and Cashman, 1996).

The statistical summary for the plagioclase crystal size data is presented in Table 3. Crystal number density (CND), the number of crystals per unit area, generally decreases from the black scoria (including plate tephra for comparison) to brown scoria. Sample BrownLL has an exceptionally large CND and the average crystal size for this sample (~4 μm) is almost half the average for the other brown scoria (7 and 9 μm). The black and brown scoria have generally concave-up crystal size distributions (CSDs), whereas the plate tephra have a kinked profile (Fig. 8). The plate tephra have a significant component of larger crystal sizes, which manifests as another kink in the CSD; it is unclear to what extent this might be a sampling artifact. However, the plate tephra formed from ruptured bubble films, probably from magma that resided near the conduit margins (Ruth and Calder, 2014). Magma near the conduit margins likely had the longest residence times, thus producing the highest crystallinities and largest crystals. One sample of brown tephra, brn1, exhibits textures similar to that of the black scoria, which could suggest it is a transitional texture. The concave-up distribution has been attributed to super exponential

453 nucleation events (i.e. growth rate is a function of crystal size; Marsh, 1998) while a kinked
454 profile is commonly observed in igneous systems and interpreted as a signature of magma
455 mixing (Marsh, 1998; Higgins, 2006; Vinet and Higgins, 2010). Overall, the slope decreases
456 from the brown to black scoria and plate tephra. Similarly, plot intercepts decrease slightly from
457 the brown to black scoria and plate tephra (see Fig. 8 insets). Changes in slope can be attributed
458 to increased residence time and/or coarsening (Higgins, 2006). Plot intercepts are not expected to
459 change with increased residence time, however they do decrease with coarsening (Vinet and
460 Higgins, 2010). BrownLL has the highest intercept of all the tephra, which combined with the
461 high crystal number density, suggests a rapid nucleation event. Since the plot intercepts decrease
462 in these datasets, the change in slope might result from coarsening via Ostwald ripening. Both
463 plate tephra and one black scoria (1Black) samples show a kink in their CSD at the smallest
464 crystal sizes, which is not observed in the brown or black scoria. This extra kink could suggest
465 that these samples may have experienced coarsening with a nucleation event right before
466 eruption. Similar distributions and interpretations were presented theoretically (Marsh, 1998) and
467 in samples from Soufrière Hills volcano (Higgins and Roberge, 2003).
468
469 # GEOCHEMICAL RESULTS
470 **Whole Rocks - Major Elements**
471 The whole rock composition of the tephra produced during the 2008 eruption is basaltic
472 with ~51 wt% of SiO_2 (n=5 whole rock samples), consistent with previously reported whole rock
473 chemistry from recent Llaima products (Naranjo and Moreno 2005; Reubi et al., 2011; Bouvet de
474 Maisonneuve et al., 2012a). These and additional geochemical data are provided in the
475 supplemental material. The black scoria samples have SiO_2 values of 51.2 to 51.59 wt%; brown

476 scoria samples have similar SiO_2 values, at 51.20 to 51.22 wt%. These data suggest, unlike the
477 textural data, that there is no discernible geochemical difference in whole rock chemistry
478 between the black and brown scoria. This finding is consistent with texturally bimodal tephra
479 reported elsewhere (e.g. Métrich et al., 2010; Cimarelli et al., 2010).
480
481 **Phenocrysts - Major Elements**
482 Mineral chemistry was determined on the phenocryst phases, the plagioclase
483 microphenocrysts, and all phases in the glomerocrysts (Table 4). The composition of the isolated
484 plagioclase phenocrysts and microphenocrysts ranges from An_{85-65} with an average of An_{69} (Fig.
485 9). Isolated olivine phenocryst compositions range between Fo_{83-66}. Plagioclase within the Cr-
486 spinel-free troctolite glomerocrysts ranges from An_{92-65}, whereas the plagioclase in the Cr-spinel
487 troctolite glomerocrysts is slightly more calcic at An_{92-75}. Olivine composition within both types
488 of glomercrysts clusters around Fo_{81}. Zoning information is limited to a small subset (n=14) of
489 olivine crystals; these are dominantly reversed zoned, which is consistent with previously
490 reported observations (Bouvet de Maisonneuve et al., 2012a). The spinel phase is Cr and Al-rich
491 with Cr# (molar $Cr/(Cr+Al+Fe^{3+})$) ranging from 26-37. Cr-spinel in conjunction with high An
492 plagioclase is consistent with origins in the deeper part of the magmatic plumbing system (e.g.
493 Streck et al., 2002). Conversely, the lack of spinel and slightly lower An plagioclase in the Cr-
494 spinel-free troctolite glomerocrysts is consistent with origins in the shallower parts of the
495 plumbing system.
496
497
498

Post Entrapment Modification of Melt Inclusions and Fe Oxidation State

Melt inclusions may experience compositional modification after trapping. Processes may include crystallization, melting, re-equilibration with the host mineral, and elemental diffusion through the host mineral (for a review, see Kent, 2008). In order to undertake meaningful analysis of the data, estimating the extent of these modifications is important.

Post entrapment modifications through Fe loss or crystallization were determined by comparing the Fe-Mg exchange coefficients (K_D) of the melt inclusion and host olivine (Putirka, 2008) (Fig. 10). Melt inclusion compositions were corrected for post entrapment crystallization by adding host olivine in 0.01% increments until $K_D(Fe^{2+}\text{-}Mg)^{ol\text{-}liq} = 0.3$ (Roeder and Emslie, 1970) using the Ford et al. (1983) olivine-melt model in the PETROLOG 3 software package (Danyushevsky and Plechov, 2011). $Fe^{3+}/\sum Fe$ ratios were measured via XANES on two melt inclusions; blk3-2011 yielded 0.194 ± 0.002 whereas blk1-2010 was 0.163. These values were used for post entrapment corrections for these samples. For samples that were not analyzed with XANES, our post entrapment crystallization (PEC) corrections assumed an oxygen fugacity equivalent to the nickel-nickel oxide (NNO) oxygen buffer typical of arc systems (Toplis and Carrol, 1995) and a $Fe^{3+}/\sum Fe$ ratio of 0.2, based on literature values for other arc systems (e.g., Cervantes and Wallace, 2003; Lloyd et al., 2013). We tested this assumption using equation 7 from Kress and Carmichael (1991) to estimate the oxygen fugacity buffer with a range of $Fe^{3+}/\sum Fe$ values (Table 5). When 20% Fe is Fe_2O_3, the buffer is ΔNNO +0.06 to +0.14 for the samples shown. At $Fe^{3+}/\sum Fe$ = 15%, the buffer is much closer to ΔNNO (-0.72 to -0.63), or ΔQFM. The buffer did not change considerably with changing pressures in the model. Under this assumption, most samples experienced < 10% post entrapment crystallization.

We assessed Fe loss to the host crystal (e.g. Danyushevksy et al., 2000) by comparing the FeO* and Mg# of the melt inclusions (anhydrous, normalized data) to the FeO* and Mg# trend of whole rock samples (Fig. 11). Melt inclusion compositions are consistent with the whole rock array, but extend to significantly more mafic compositions. Four samples showed evidence of post-entrapment Fe-loss. These inclusions were all less than 40 microns, considerably smaller than other melt inclusions in the suite, which ranged from <20 to 425 microns in diameter (average 68 μm). As such, they could re-equilibrate faster than larger melt inclusions and therefore, their measured compositions may not reflect actual magmatic compositions (Cottrell et al., 2002). Due to well documented post entrapment complications from Fe-loss (e.g. Danyushevsky et al., 2000), these melt inclusions were filtered from the suite.

Water concentrations in olivine-hosted melt inclusions may be affected by post entrapment diffusion of H, and possibly molecular water, through the olivine crystal lattice (Métrich and Wallace, 2008; Johnson et al., 2008; Portnyagin et al., 2008). Three lines of evidence argue against significant diffusive water loss from the majority of our inclusions. First, significant water loss may cause extensive (>10%) post entrapment olivine crystallization by increasing the inclusion liquidus temperature (Lloyd et al., 2013; Bucholz et al., 2013). We therefore do not include any inclusions with > 10 % post-entrapment crystallization in this study. Second, H loss may initiate precipitation of fine magnetite within the melt inclusion (Danyushevsky et al., 2002; Métrich and Wallace, 2008), though this has been contested in other studies that propose that proton diffusion into the inclusion is rapid and would mitigate any changes in oxidation state (Gaetani et al., 2012; Bucholz et al., 2013). We do not include any inclusions with daughter crystals in this study. Third, comparisons of olivine-hosted melt inclusions sourced from ash, lapilli, and bombs show that samples sourced from lapilli, such as

544 those we report on here, may experience limited amounts of water diffusion (Lloyd et al., 2013).
545 We consider diffusive water loss minimal, though it cannot be entirely excluded. In summary,
546 going forth we consider only glassy melt inclusions that are free of daughter crystals although
547 vapor bubbles may be present, are without significant Fe loss, and have less than 10% post
548 entrapment crystallization.

549 Recent studies have shown that CO_2 concentrations in melt inclusions are also altered by
550 post-entrapment processes (e.g. Neave et al., 2014; Wallace et al., 2015; Aster et al., in
551 preparation). In particular, post-entrapment modifications of the melt inclusion via cooling and
552 crystallization causes a decrease in pressure. CO_2 partitions into the resultant vapor bubble
553 because of the pressure dependence of its solubility. This can be augmented if there is H^+ loss via
554 diffusion into the host mineral. Ultimately, these processes lower the CO_2 content of the melt
555 inclusion by as much as 40 to 90% (Wallace et al., 2015; Aster et al., 2016). Recovering the
556 original CO_2 contents of the melt inclusion requires knowing the volume of the vapor bubble and
557 the CO_2 density within the bubble; however, we do not have these data for our suite of
558 inclusions. Alternatively, original melt inclusion CO_2 contents may be estimated assuming that a
559 bubble forms during thermal contraction associated with crystallization and cooling (Aster et al.,
560 2016); the bubble volume can be estimated with crystallization and thermal contraction models.
561 However, this correction assumes that the olivine have higher entrapment temperatures than
562 eruption temperatures. Of the 182 melt inclusions analyzed in this study, entrapment
563 temperatures were lower than eruption temperatures for 171 melt inclusions (calculated using the
564 technique outlined in Aster et al. (2016)). These melt inclusions are less likely to have
565 experienced thermal contraction. This suggests that the Aster et al. (2016) protocol may not be
566 appropriate for these samples. We report uncorrected CO_2 values and consider these as minima.

Major Elements in Melt Inclusions

Our melt inclusion dataset show a wide compositional range, with the most mafic and most evolved compositions between 49 and 56 wt% SiO_2 respectively, expanding on the previously reported compositional range (Bouvet de Maisonneuve et al., 2012a) (Table 6). The matrix glasses show similar trends to the melt inclusions, but with a smaller range of values for all elements (e.g., 52 - 55 wt% of SiO_2). The majority of the samples (152 of 182 melt inclusions) are consistent with a single liquid line of descent (LLD) fractionating of olivine and plagioclase (Fig. 12). CaO and Al_2O_3 trends do not change slope with respect to SiO_2, suggesting that clinopyroxene did not crystallize during the evolution of the melt. These observations are consistent with sample petrography, as the dominant phenocryst assemblage is plagioclase + olivine. MnO and FeO^T (i.e. FeO + $0.8998Fe_2O_3$) do not exhibit obvious trends with respect to SiO_2. Na_2O and K_2O behave as incompatible elements for the range of SiO_2 presented, all increasing with increasing SiO_2 content.

We observe a tight LLD for TiO_2 and P_2O_5 vs SiO_2 < 52 wt%. After 52 wt% SiO_2, we observe a factor of five range in TiO_2 and P_2O_5 values, falling into three groups (see Fig. 12). One group follows the main LLD. The second group shows decreasing TiO_2 and P_2O_5 (23 of 182 melt inclusions). For this subset, Al_2O_3 and Na_2O show slightly elevated concentrations with respect to the main LLD. These findings are consistent with localized assimilation of a lithology more evolved than the main LLD, possibly Tertiary intrusives (e.g. Lucassen et al., 2004) or evolved ancestral magmas potentially with Ti-magnetite (Reubi et al., 2011). A third group shows higher values of TiO_2 and P_2O_5 (7 of 182 melt inclusions). These samples also have some of the lowest CaO, Al_2O_3, and Na_2O concentrations in the dataset. These data are consistent with

590 formation in a residual, interstitial melt in the crystal mush (e.g. Bouvet de Maisonneuve et al.,
591 2012a).

592 The P_2O_5 values reported here are significantly higher than those reported in Bouvet de
593 Maisonneuve et al. (2012a) (see Fig. 12). Our melt inclusion data are consistent with observed
594 matrix glass and whole rock trends. Additionally, the whole rock values for P_2O_5 reported by
595 Bouvet de Maisonneuve et al. (2012a) overlap with the whole rock P_2O_5 values reported in our
596 study. These differences could be attributed to differences in analytical methodology such as
597 count times, or primary standards.

598 The chemical compositions of melt inclusions sourced from the black and brown scoria
599 overlap (Fig. 13); therefore, in this study we treat the melt inclusions as a single set. This
600 observation contrasts with those of Métrich et al. (2010), who propose, for the Stromboli system,
601 that olivine sourced from Stromboli brown scoria (i.e., "golden pumice" in their paper) originate
602 from a different magma than their black scoria.

603

604 **Olivine-Hosted Melt Inclusion Trace Elements**

605 The multi-element spider plot (Fig. 14) shows the range and average of key elements
606 including select rare earth elements (REE) and large-ion lithophile elements, which are used to
607 infer information about petrogenetic processes. All data collected with LA-ICPMS are plotted
608 and overlain by the calculated average value; we also included results from previously reported
609 whole rock trace element data from Llaima Holocene tephras for comparison (dark gray region;
610 Jacques et al., 2014). Our trace element data show a signature generally consistent with
611 subduction zone magmas as evidenced by enrichments of fluid-mobile elements (e.g., Rb, Ba, K,
612 U, Pb), a negative Nb-Ta anomaly, and moderately enriched light REE with respect to heavy

613 REE, as previously reported elsewhere (e.g. Hickey-Vargas et al., 1986; Reubi et al., 2011;
614 Jacques et al., 2014). However, several elemental signatures do exhibit some notable variation
615 from those data in the literature. First, we observe positive Eu anomalies in some of our melt
616 inclusions, and negative Eu anomalies in others. Second, Ba/La in our dataset ranges from 17-46,
617 whereas literature values for Llaima range from 23-27 (e.g., Reubi et al., 2011; Jacques et al.,
618 2014). Similarly, the range of observed Nb-Ta anomalies is wider than previously reported (see
619 Fig. 14). Conversely, Ce/Pb values in our samples (2-4) overlap well with literature values (2-3)
620 (Reubi et al., 2011; Jacques et al., 2014).
621
622 **Volatiles in Melt Inclusions and Matrix Glass**
623 Volatile contents within the melt inclusions were measured with the methodologies
624 discussed earlier; the results are shown in Table 6. H_2O and CO_2 were not measured in the matrix
625 glass because it was not possible to prepare FTIR wafers without crystals that interfered with the
626 path of the IR beam. S and Cl in the matrix glass were measured with EMPA and range from 6-
627 600 ppm and 330 – 500 ppm, respectively.
628 FTIR results for H_2O in the melt inclusions range from 0.36 to 2.97 wt%. Similarly, the
629 SIMS analytical results have H_2O contents ranging from 0.57 to 2.37 wt% H_2O. H_2O values
630 correspond with those reported in previous work (Bouvet de Maisonneuve et al., 2012a) (Fig.
631 15). CO_2 values from the FTIR analysis range from 397 to 1973 ppm, contrasting with the lower
632 CO_2 from SIMS analysis (22 to 274 ppm). We would expect the FTIR analysis to record the
633 lower CO_2 contents. However, many of our samples exhibited fringes (e.g. Nichols and
634 Wysoczanski, 2007), the presence of which could have obscured the small CO_3^{2-} doublet that

635 would result from low CO_2 in the melt inclusions. The CO_2 values presented here are the highest
636 measured in recent Llaima samples to date.

637 Sulfur contents from the EPMA analyses range from 23 to 1534 ppm. SIMS analyses
638 report sulfur abundances from 92 to 1277 ppm. Similarly, chlorine results from EPMA show
639 concentrations from 47 to 1342 ppm, whereas SIMS results have abundances from 236 to 641
640 ppm.

641 We were unable to measure volatiles using all techniques on each melt inclusion, thus
642 direct comparisons between the techniques were not possible with this dataset. However, the
643 measured values from the SIMS for H_2O, S, and Cl overlap well with those reported from EPMA
644 and FTIR (see Table 6). For S and Cl, the EPMA results show a wider range of values compared
645 with the SIMS results. Similarly, the range of FTIR H_2O concentrations is wider than those
646 obtained via SIMS. CO_2 concentrations measured using SIMS were lower, on average, than
647 those measured using FTIR; however, we were only able to retrieve CO_2 values using FTIR from
648 12 samples.

649

650 **Entrapment and Magma Temperature Calculations**

651 Entrapment temperature for each melt inclusion-olivine pair was estimated using olivine-
652 liquid equilibria, which is based dominantly on the Mg partitioning behavior between olivine and
653 the melt and has been calibrated for hydrous melts (Putirka et al., 2007; Putirka et al., 2008). For
654 this study, we used equation 22 from Putirka (2008), which includes the effect of H_2O on the
655 temperature calculation. H_2O contents measured with FTIR or SIMS were included for the
656 respective melt inclusions. We assumed an anhydrous melt for those melt inclusions without
657 H_2O content data. Using Equation 22 from Putirka (2008), the melt inclusion entrapment

temperatures ranged from 1094 °C to 1233 °C, with an average of 1175 °C. This range of entrapment temperatures strongly suggests that olivine grew in a wide variety of magmatic thermal conditions, and that cooling-induced crystallization was likely an important process.

To further constrain magmatic temperatures in the shallow plumbing system, plagioclase-liquid equilibria, based on the alkali/alkali earth partitioning between the plagioclase and the melt (Putirka, 2008) was also considered. Assuming equilibrium and using the composition of the microphenocryst plagioclase and the anhydrous matrix glass, we estimated the average temperature just prior to eruption at 1146 °C (low 1109 °C, high 1167 °C). We compared these magmatic temperatures with those calculated from the plagioclase hygrometer proposed by Lange et al., (2009). Using the matrix glass H_2O values (0.88 wt%, rounded to 0.9 wt% - Bouvet de Maisonneuve et al, 2012a), the average matrix glass composition (SiO_2: 53.36 wt%, TiO_2: 1.34 wt%, Al_2O_3: 15.56 wt%, FeO^T:10.69 wt%, MgO: 5.69 wt%, CaO: 8.91 wt%, Na_2O: 3.18 wt%, K_2O: 0.76 wt%), the average plagioclase composition (An_{69}), and pressure at 50 MPa, we calculated the minimum shallow magmatic temperatures as 1115 °C. This is lower than the results from the Purtirka model, but within the range of expected uncertainty (±25-30 °C) for geothermometers in general (Putirka, 2008). Based on this, we assume the calculated 1146 °C temperature as a maximum magmatic temperature.

Melt Inclusion Entrapment Pressures

The pressure-dependent solubility behavior of CO_2 and H_2O can be used to estimate the entrapment pressures of the individual melt inclusions (Dixon et al., 1995; Métrich and Wallace, 2008). That H_2O and CO_2 vary widely in our melt inclusions indicates melt inclusion formation (and associated olivine crystallization) occurred over a wide range of pressures. Two solubility

models have been commonly used to estimate entrapment pressures: VolatileCalc (Newman and Lowenstern, 2002) and the Papale et al. (2006) model. Moore (2008) established that the Papale model was the best choice for calc-alkaline magmas because VolatileCalc neglects the effect of Ca on CO_2 solubility. Note that we did not correct for the possible CO_2 migration into vapor bubbles in the melt inclusions and, therefore, consider these values as minimum entrapment pressures. The entrapment pressures for our suite of melt inclusions range from 8 to 342 MPa, based on the Papale model (Fig. 15). Assuming a crustal density of 2500 kg m^{-3}, depths range between ~340 m and 13.9 km. We observe a strong peak between 50-100 MPa (1-4 km), suggesting a crystal rich region (i.e. the crystal mush). These data increase the depth of the crystallizing portion of the plumbing system as reported by Bouvet de Maisonneuve et al. (2012a) by a factor of three.

DISCUSSION

System Wide Processes

Magmatic Evolution

The majority of our dataset shows evidence for a connected magmatic system that fractionates olivine + plagioclase. The most primitive melt inclusions follow the main liquid line of descent (LLD) (see Fig. 12). More compositional variability is observed in melt inclusions with > 52 wt% SiO_2. Low TiO_2 melt inclusion compositions are most consistent with assimilation of more evolved lithologies, probably with SiO_2 values between 56-58 wt% and very low TiO_2 and P_2O_5. These could represent the basement Teritary intrusives (e.g. Lucassen et al., 2004) or evolved ancestral magmas (Reubi et al., 2011). Positive Eu anomaly values (1.10 ±0.24) are indicative of plagioclase dissolution which supports assimilation. This assimilation

704 occurred within the inferred crystal mush zone as evidenced by entrapment pressures ranging
705 from 50 to 150 MPa. Our interpretation is consistent with previous work that suggests limited
706 assimilation occurs potentially as a late-stage shallow process (e.g. Reubi et al., 2011).

707 The high TiO_2 melt inclusions have elevated P_2O_5 and K_2O, and low values of Al_2O_3 and
708 CaO. Eu anomaly values average 0.77 ± 0.05, indicative of plagioclase fractionation. These data
709 are consistent with melt inclusion formation in melts that fractionated a higher modal abundance
710 of plagioclase than the main LLD inclusions. We propose that these melt inclusions formed from
711 interstitial melts in crystal rich regions in the plumbing system (e.g. Bouvet de Maisonneuve et
712 al., 2012a). Only two melt inclusions from the high TiO_2 group have pressure estimates and these
713 are 73 and 309 MPa, respectively. The latter entrapment pressure possibly suggests that crystal
714 rich zones with evolved interstitial melts may be present in the deep system, as well as the crystal
715 mush. Although we cannot quantitatively link the number of melt inclusions to magma volumes,
716 the large number of melt inclusions analyzed (n=182) suggests that melt inclusions from the high
717 TiO_2 (n=7, 3.8% of the sample suite) and low TiO_2 (n=23, 13% of the sample suite) groups both
718 represent volumetrically minor amounts of magma compared to the main LLD. Our dataset
719 contrasts with previously reported interpretations that suggest melt inclusions dominantly formed
720 in isolated melts with different evolution histories (Bouvet de Maisonneuve et al., 2012a).
721
722 *Degassing and Crystallization*
723 The melt inclusions display a wide range of CO_2 contents, from below detection to nearly
724 2000 ppm, but tightly cluster near 2 wt% water down to CO_2 contents of ~100 ppm. The
725 population of inclusions with CO_2 below 100 ppm and with 2 wt% water argues for open system
726 degassing (Fig. 15). In this work, we understand open system degassing as the process in which

volatiles exsolve, decouple from the parent magma and then escape through bubble ascent (i.e. fractional degassing) (Dixon and Stolper, 1995; Cashman, 2004). Our findings contrast with previous studies that suggest that explosive eruptions in mafic systems result from rapid magmatic ascent under closed system degassing conditions (e.g. Coltelli et al., 2005; Métrich and Wallace, 2008). For example, paroxysmal eruptions (i.e. violent Strombolian) at Stromboli show distinctly different degassing trends (Fig. 15a), which have been interpreted to record closed system degassing and ascent (Métrich et al., 2010). In closed system degassing, volatiles exsolve to form a vapor phase, and then remain with the parent melt (i.e. equilibrium degassing). When ascent is rapid, the vapor phase increases in volume fraction, and as it is coupled to the magma, it leads to explosive fragmentation. Although, passive degassing processes at the summit have been linked elsewhere to both open and/or closed system degassing processes in deeper plumbing systems (e.g. Burton et al., 2007), the melt inclusion evidence for open system degassing at Llaima indicates that volatiles, even at depth, are decoupled from the magma, and allowed to ascend. Therefore, to produce the 2008 violent Strombolian eruption, a mechanism must be invoked which can explain the observed transition from passive degassing to explosive activity, but is independent of the established deeply-rooted passive degassing system.

Water loss through degassing promotes crystallization (e.g. Crabtree and Lange, 2011; Applegarth et al., 2013). Although crystallization does occur during syn-eruptive cooling and degassing, melt inclusion entrapment in olivine is not likely to occur syn-eruption. We explored the relationship between degassing and crystallization by comparing the respective proxy ratios (e.g. Blake et al., 2010; Johnson et al., 2010). Figure 16 displays the volatile/K_2O ratios for H_2O, S, Cl, and CO_2 versus MgO/K_2O. If crystallization occurred without degassing, the data would follow a horizontal trend. If degassing was dominant, the data would follow vertical trend. Our

750 results show strong correlations between MgO/K_2O and H_2O/K_2O, Cl/K_2O, and S/K_2O,
751 indicating that degassing and crystallization are coupled processes. CO_2/K_2O correlated with
752 MgO/K_2O at lower CO_2 values (i.e. lower pressures), but do not correlate at higher CO_2 values.
753 Indeed, the majority of the sample suite falls on the coupled crystallization and degassing trend,
754 including samples with high volatile contents (e.g. high volatile/K_2O ratios). Similarly, scoria
755 matrix glass values fall on the trend with some of the lowest S/K_2O and Cl/K_2O values in the
756 dataset. This indicates that the matrix glass was almost completely degassed due to
757 crystallization. Some melt inclusions have similarly low S/K_2O values, suggesting that the melt
758 inclusions trapped largely degassed magma. These inferences suggest that crystallization and,
759 importantly, degassing were coupled in the deep plumbing system (at least to 14 km depth), as
760 well as the shallow system. These data combined with the wide range of olivine entrapment
761 temperatures suggest that cooling-induced and degassing-induced crystallization processes may
762 be equally important.
763
764 **Shallow System Processes – Passive Degassing**
765 *Textural Maturation and the Formation of Black and Brown Scoria*
766 The brown scoria exhibit textural data indicative of rapid nucleation at relatively high
767 undercooling, i.e. higher intercept on the CSD plot and high vesicle number density. The inferred
768 initial stages of vesicle ripening in the brown scoria likely occurred during ascent in the conduit
769 just before quenching. Similar interpretations and short timescales were presented for vesicle
770 ripening in reticulite from Hawaii (e.g. Mangan and Cashman, 1996). Conversely, textural data
771 from the black scoria suggest a rapid nucleation event but also more prolonged crystal growth,
772 while vesicle textures suggesting steady-state nucleation with possibly some coalescence. These

773 data are indicative of longer residence times before eruption. Together, the observed textures are
774 indicative of a continuum of textural maturation from the brown to black scoria that we propose
775 results from background passive degassing. The presence of normally-zoned microphenocryst
776 plagioclase predominantly in the black scoria supports this, as it suggests growth-dominated
777 conditions associated with lower, possibly steady-state, rates of degassing (Cashman, 2004;
778 Castro et al., 2005). In summary, the textural features of the black scoria reflect passive
779 degassing conditions in the conduit and likely represent magma slowly circulating within the
780 shallow plumbing system.

781 Texturally bimodal scoria were first observed and described at Stromboli (Francalanci et
782 al., 2004) and have since been observed in other systems (e.g. Croscat complex cone system –
783 Cimarelli et al., 2010). The formation of texturally bimodal scoria in explosive systems has been
784 attributed to two processes, depending on whether they are geochemically distinct, or not. Where
785 scoria originated from geochemically-similar magma sourced from similar locations within the
786 shallow plumbing system, textures are interpreted to record end members on a textural maturity
787 continuum (Lautze and Houghton, 2007; Erlund et al., 2010; Cimarelli et al., 2010). In these
788 cases, differences among scoria types are a function of the physical processes experienced.
789 Alternatively, where distinctions can be made in the geochemistry, such as melt inclusion
790 chemistry, the source magmas for the different scoria are chemically distinct and originate from
791 different locations in the system (Métrich et al., 2001, 2010). At Llaima, the geochemical
792 similarity of the scoria whole rock compositions (Fig. 12) and the fact that melt inclusions from
793 the different scoria overlap (Fig. 13) indicate that differences are textural alone, and likely
794 formed as a result of differing degassing histories, rather than from geochemically different
795 magmas (at least with respect to major element chemistry).

Plumbing System Conceptual Model

Summarizing the scoria textures, olivine hosted melt inclusions, as well as findings from previous work (e.g. Bouvet de Maisonneuve et al., 2012a, 2012b, Ruth and Calder 2014) we present here a conceptual model of the plumbing system at Llaima from the vent to ~14 km depth (Fig. 17). We infer two magma accumulation regions based on the clustering of melt inclusion entrapment pressures (histogram in Fig. 15). The main magmatic region is the shallowest, extending from the conduit (300 m) to ~4 km. Magma that produced the black 'resident' scoria is likely sourced from this region. Most melt inclusions formed (or re-equilibrated) at pressures from between 50-100 MPa. This strongly supports the crystal mush zone proposed in previous work (e.g. Bouvet de Maisonneuve et al., 2012a, 2012b). Crystallization of olivine and plagioclase occurred throughout the plumbing system as evidenced by the main LLD. Minor amounts of localized assimilation of evolved lithologies occurred in the crystal mush zone (e.g. low TiO_2 melt inclusions, 50-150 MPa entrapment pressures). High TiO_2 and P_2O_5 melt inclusions with similar crystal mush pressures also evidence entrapment of interstitial melts. Reverse zoning in olivine crystals suggests this as the main region of magma mixing (Bouvet de Maisonneuve et al., 2012b; Ruth, 2014). This magma mixing probably produced the multiply zoned plagioclase and the sieve textured plagioclase phenocrysts, textures which form under dynamic conditions, especially with respect to magmatic H_2O and temperature (Landi et al., 2004; Streck, 2008; Crabtree and Lange, 2011; Bouvet de Maisonneuve et al., 2012b). Since plagioclase crystals within the Cr-spinel-free troctolite glomerocrysts have similar sieve textures, we infer that they are also sourced from the crystal mush zone.

Olivine hosted melt inclusions show that the deeper plumbing system extends from 4 to 14 km depth. Although we do not have many samples from the deep system, we infer information about the processes occurring within this region from melt inclusion chemistry and the Cr-spinel troctolite glomerocrysts. Degassing occurs at up to 14 km depth, and is coupled with crystallization. Extensive crystallization is suggested by the one melt inclusion with high TiO_2 and P_2O_5 with high entrapment pressure, which may have formed in the interstitial melts within this region. Moreover, the presence of Cr-spinel in some troctolite glomerocrysts is consistent with deeper origins that have experienced limited fractionation (e.g. Streck et al., 2002); these are most likely to be found at depths lower than the main crystal mush zone. This potentially suggests a crystal rich zone in the deeper system (e.g. Annen et al., 2006). Similar crystal rich zones have been proposed for the deeper system beneath Mt. Etna (e.g. Laiolo and Cigolini, 2006).

Changes in Magmatic Physical Properties Due to Passive and Syn-eruption Degassing

Magma viscosity is affected by crystal abundance and morphology, which can be altered due to degassing processes. Analog experiments show that increasing microlite abundance with respect to phenocryst abundance can potentially increase effective viscosity by up to three orders of magnitude (Cimarelli et al., 2011). The effective viscosity may increase further as a result of syn-eruption (or passive) degassing and crystallization. Heating experiments on volatile-poor porphyritic basalts reveal that rapid, significant degassing and crystallization (up to 35%) can occur in degassed conduit melts, resulting in additional dendritic to spherulitic crystal nucleation on existing crystals (i.e. overgrowths) (Applegarth et al., 2013, see their Figure 12 and 13). We estimated the viscosity indirectly using the MAGMA software package (version 2.50.0133

841 http://www.lanl.gov/orgs/ees/geodynamics/Wohletz/KWare/Index.htm), the average whole rock
842 composition, and the average total crystallinity of the brown and black scoria (Table 8). The
843 majority of the crystallinity in both cases is microlites since the phenocryst content for both
844 scoria types is less than 10%. The brown scoria magma has a vesicle-free effective viscosity
845 ranging from 5.4×10^{1} to 1.33×10^{2} Pa s. The black scoria magma has a vesicle-free effective
846 viscosity that is generally two to three orders of magnitude higher (2.29×10^{4} to 5.64×10^{4} Pa s).
847 Our first order approximation of viscosity differences is consistent with findings reported in
848 Cimarelli et al. (2011). Additionally, in the black and brown scoria we observe dendritic
849 overgrowth textures similar to those found in Applegarth et al. (2013), especially around
850 boundaries between textural domains (Fig. 5d), and near vesicles and fractures (see supplemental
851 material Fig. S3). The proximity to vesicles, in particular, suggests formation resulting from late
852 stage degassing. Based on the experimental results from the literature and our textural data, we
853 propose that significant viscosity changes resulted from both passive degassing prior to, and syn-
854 eruptive degassing during, the 2008 eruption at Llaima.
855
856 **Transitions in Eruptive Style at Llaima**
857 Maintenance of an open conduit commonly associated with passive degassing requires
858 that heat and magma be continually replenished (Kazahaya et al., 1994; Stevenson and Blake,
859 1998). Heat and magma supply to the upper plumbing system can occur through density-driven
860 convective mixing between the degassed, and cooler shallow magmas and relatively volatile-rich
861 and hotter, deeper magmas (Kazahaya et al., 1994; Allard, 1997; Stevenson and Blake, 1998;
862 Beckett et al., 2014). An additional mechanism for inducing axial mixing which is likely to be

863 important, is that the ascending gas flux in a conduit will itself drive a return flow of magma
864 (Pansino, 2012).

865 We propose that the background activity at Llaima is maintained through periodic small-
866 batch mafic injections, as evidenced by crystal zoning, into the base of a crystal mush (1-4 km
867 depth) (Fig. 17). Resultant hybrid magmas with initially moderate H_2O content (~ 2 wt%) are
868 mobilized and entrained into the axial mixing processes. The ascent and mixing results in
869 degassing and crystallization, and we speculate that this magma would ultimately result in the
870 black scoria type products with the observed mature crystal and vesicle textures.

871 For the 2008 eruptive episode, magma injection and mush remobilization, evidenced by
872 reversely zoned olivine (e.g. Bouvet de Maisonneuve et al., 2012a,b; Ruth, 2014), have been
873 proposed as a triggering mechanism (Bouvet de Maisonneuve et al., 2012a). However, the lack
874 of significant ground deformation prior to the eruption suggests that any magma injection into
875 the system must have been volumetrically minor (Remy et al., 2015; Delgado et al., in
876 preparation). Further, violent Strombolian eruptions are highly pulsatory in nature and require
877 high mass and gas fluxes to drive them (Pioli et al., 2009). Therefore, any robust discussion of
878 the triggers of such an eruption must account for substantial gas accumulation and its rapid
879 ascent. Three mechanisms of potential gas accumulation are discussed below:

880 (i) Crystal mush zones may facilitate gas accumulation. Analog experiments suggest that
881 small vesicles can become trapped within particle-rich suspensions (i.e. gas holdup), which may
882 regulate gas flux through the plumbing system (Belien et al., 2010; Tran et al., 2015).
883 Populations of small vesicles can be added to the crystal mush through volatile saturation and
884 subsequent nucleation. A crystal mush zone at Llaima is inferred at depths between 1 and 4 km,
885 based on the melt inclusion entrapment pressures. With the average whole rock composition, and

886 2 wt% H_2O, saturation pressures (calculated with Papale et al. (2006)) are between 70 and 80
887 MPa (~ 3 km depth), thus it would be reasonable to expect vesicle nucleation within this region.
888 Cr-spinel-free troctolite glomerocrysts have matrix glass with vesicles, lending further support to
889 this hypothesis. These vesicles may have formed during syn-eruption ascent, but their convoluted
890 morphologies suggest some maturity. Further, ascending CO_2-rich vesicles from depth may also
891 be partially trapped in the crystal mush (Thomas et al., 1993; Costa et al., 2006). The passive
892 degassing behavior at the summit and the open system degassing signature of the melt inclusions
893 indicate that gas bubbles within the system are mobile. Some mobility may occur due to crystal
894 settling within the mush (e.g. Boudreau, 2016), with some bubble ascent feeding the passive
895 degassing. However, significant bubble ascent might be inhibited by the surrounding crystals.
896 We propose that gas accumulates within the mush until a critical gas volume is reached. Once
897 the bubbles are released from the crystal mush via remobilization (i.e. unlocked) the accumulated
898 gas would ascend rapidly to generate explosive activity (e.g. Vergniolle and Jaupart, 1990;
899 Parfitt and Wilson, 1995).

900 (ii) Extensive passive degassing could result in increased viscosity for magma residing
901 within the upper conduit. Over time, this magma would stagnate and potentially form a
902 rheologically stiffer (but still permeable) cap, above which magma circulation does not take
903 place. Experimental work suggests that rheological barriers lead to elevated gas overpressures,
904 ultimately increasing the intensity of Strombolian eruptions (Del Bello et al., 2015). Although we
905 do not have direct evidence for such rheological barrier, the black scoria and plate tephra from
906 the 2008 eruption have textures consistent with prolonged residence and slightly higher
907 viscosities (relative to crystal-free magmas of the same composition), as implied by their higher
908 crystallinities (Table 8). Moreover, with increased viscosity, vesicle coalescence and growth

could be retarded (Cashman, 2004; Tran et al., 2015) further augmenting gas accumulation beneath the barrier.

(iii) Complex plumbing system geometry involving sills could provide additional traps for gas accumulation. Experimental results indicate that sills in passively degassing systems may serve as effective traps by segregating gas via buoyant exchange flow between the sill and conduit (Menand and Phillips, 2007). The plumbing system geometry of Llaima is not well constrained. Regional tectonics and the alignment of vents may indicate that the plumbing system follows a NE-SW orientation (Cembrano and Lara, 2008; Schonwalder-Angel, 2015). However, there is limited discussion of sills and/or other sub-horizontal bodies. Recent studies using InSAR inferred the presence and inflation (6-15 cm) of a sill to the west of the summit at ~ 5 km depth prior to a subsequent explosive phase on 3 April 2009 (Delgado et al, in preparation); there is assumed post-eruptive subsidence after this event. Although inflation was not observed before the 2008 eruption, the findings in Delgado et al. (in preparation) do suggest that a potential short-lived trap for magma and gas accumulation could have occurred.

We propose the following scenario to explain the transition to the violent Strombolian eruption at Llaima on 1 January 2008 (Fig. 17). The eruption occurred in a system that was already passively degassing which was likely sustained by repeated, minor, magma injection events. Upon injection these magma batches degassed volatiles that partially filtered through the crystal mush. Simultaneously, some of these volatiles, as well as volatiles ascending from depth, accumulated in the mush and under the stiffened conduit magma until a critical gas volume was reached. Disruption and remobilization of the mush by injecting magmas unlocked the accumulated gas phase, which ascended rapidly to generate the explosive activity at the vent. Clearing the upper portions of the shallow magma reservoir allowed rapid, and likely chaotic,

ascent of the deeper, relatively volatile-rich, magma from depths up to 14 km. Partial mixing between the influx, crystal mush and the resident magma produced the glomerocrysts and the crystal-rich domains represented by the clots of black scoria in the brown scoria (Fig 5b). Thus magma injection and gas accumulation processes equally contributed to eruption triggering.

Explosive Eruptions in Mafic Systems

Explosive mafic eruptions are commonly associated with closed system degassing and ascent of magmas from depth (e.g. Roggensack et al., 1997; Métrich et al., 2010). Bouvet de Maisonneuve et al. (2012a, 2012b) suggest that the dominant cause of the 2008 explosive eruption of Llaima was injection-related, heat-induced rheological changes in a crystal mush. We agree with Bouvet de Maisonneuve et al. (2012a, 2012b) that magma injection is an important contribution in triggering the eruption. However, the injection and remobilization model alone does not fully explain transitions from passive summit degassing that continuously leaks gas to an explosive eruption characterized by pulsatory behavior that must be related to gas accumulation (Pioli et al., 2009). Previous studies of mafic volcanoes elsewhere highlight the importance of accumulated gas in producing explosive and pulsatory behavior (e.g. Andronico et al., 2009; Pioli et al., 2008; Belien, 2011; Preece et al., 2016). Gas accumulation within crystal mushes has been invoked to explain eruptive behavior in intermediate to silicic systems (Sisson and Bacon, 1999; Pistone et al., 2015; Edmonds et al., 2016). We would have more insight into this process if comparable studies of gas accumulation within mafic systems were available. Additionally, magma reservoirs with accumulated gas are more compressible, and thus able to accommodate more influx with limited ground deformation (Voight et al., 2010); this could explain the lack of observed ground deformation prior to the 2008 activity. Therefore, we posit

955 that gas accumulation within the crystal mush, as well as other traps within the upper plumbing
956 system, and its subsequent sudden disruption and ascent is an equally important contribution to
957 eruption triggering. The proposed mechanism provides an alternative means for mafic systems to
958 generate explosive eruptions that does not rely on rapid ascent of magmas under closed system
959 degassing conditions. This is especially pertinent for understanding major explosive eruptions in
960 mafic systems like Llaima that exhibit a dominantly, open system degassing signature.
961

962 ## CONCLUSIONS

963 We conducted an extensive geochemical and textural study of the products from the 2008
964 eruption of Llaima. Our aim was to establish how the processes associated with the explosive
965 eruption initiate and occur, specifically in the context of the established background passive
966 degassing of the system. Here we present the three main conclusions from this work.

967 1. Texturally bimodal scoria were observed and analyzed. Crystal and vesicle size
968 distributions reveal quantitative texturally differences between the "brown" and "black"
969 scoria from the 2008 eruption of Llaima Volcano. The black scoria samples generally
970 have higher crystal number densities and larger vesicles, whereas the brown scoria have
971 lower crystal number densities and smaller vesicles. Overall, this suggests increasing
972 textural maturation from the brown to the black scoria. Black scoria likely formed from
973 magma that experienced prolonged passive degassing and crystallization in the shallow
974 conduit whereas the brown scoria is characterized by features resulting from rapid syn-
975 eruptive ascent, degassing and crystallization.
976 2. Our dataset provides the first evidence for an extended deep, mafic plumbing system with
977 olivine-hosted melt inclusions that sampled magmas that range from 49 to 56 wt% SiO_2

at pressures from 8-342 MPa (300 m to ~ 14 km). The majority of samples formed at pressures between 50 and 100 MPa, consistent with a shallow crystal mush. Major elements record a main LLD consistent with plagioclase and olivine fractionation in a well-connected system. Two smaller groups of melt inclusions show higher and lower TiO_2 and P_2O_5 with respect to the main LLD. Low TiO_2 and P_2O_5 samples suggest localized assimilation of more evolved lithologies. The high TiO_2 samples may have formed in isolated pockets of evolved melt; they form at high and low pressures suggestive of extensive crystallization throughout the system. H_2O and CO_2 in the majority of the melt inclusions show evidence for open system degassing, which is coupled with crystallization throughout the system.

3. Based on the combined textural and geochemical data, we propose that the main magmatic locus is a crystal mush, located between 1 and 4 km depth. Small volumes of magma from the deeper system are periodically injected, quasi steady state, into the shallow system. This contributes to maintaining passive degassing at the summit. We propose that concurrent with the passive degassing, gradual gas accumulation in the crystal mush and below the rheologically stiffer upper conduit magma occurred over time such that a critical gas volume in the system was reached, and the system overpressure was surpassed by magma injection prior to the 2008 eruption. Magma remobilization unlocked the accumulated gas, which was able to ascend rapidly and generate the observed explosive and pulsatory activity at the summit. Our proposed scenario provides an alternative model to those that posit that explosive mafic volcanism results from rapid ascent of magma due under closed system degassing conditions. This mechanism

provides a means for systems with dominantly open system degassing behavior to transition from passive degassing to violent explosive eruptions.

ACKNOWLEDGEMENTS

We thank D. Schonwalder-Angel, E. Breard, R. Leach, P. Whelley, and A. Brownell for help in the field, and C. Bouvet de Maisonneuve, O. Bachmann, M. Brounce, J. Ball, A. Graettinger, and G. Valentine for helpful discussions. T. Gooding helped immensely with sample preparation. T. Rose and S. Lynton helped with data collection at the Smithsonian. M. Lytle helped with the LA-ICPMS analyses. J. Herrin aided with the spinel analyses at Nanyang Technological University. N. Shimizu and B. Monteleone aided with the SIMS measurements. M. Ruth wrote the MATLAB script to correct for fringes in the FTIR spectra. This work was funded by the Geological Society of America [Graduate Student Research Grant to D.C.S.R]; the Smithsonian Institution [Graduate Fellowship to D.C.S.R]; the Society of Economic Geology [Hugh McKinstry Student Research Grant 11-85 to D.C.S.R.]; and the National Science Foundation [EAR-0828070 to E.S.C. while at the University at Buffalo]. The ion microprobe facility at the Northeast National Ion Microprobe Facility at Woods Hole Oceanographic Institution was partially subsidized by the Instrumentation and Facilities Program, Division of Earth Sciences, National Science Foundation. We thank D. Geist, T. Hansteen, and two anonymous reviewers for constructive and helpful comments. We finally thank Marjorie Wilson for her editorial help and patience during the revision process.

REFERENCES

Abbey, S. (1983). Studies in "Standard Samples" of Silicate Rocks and Minerals 1969-1982, *Canadian Geological Survey,* 83-15, p. 114.

Allard, P. (1997). Endogenous magma degassing and storage at Mount Etna. *Geophysical Research Letters,* 24 (17), 2219-2222.

Andronico, D., Cristaldi, A., Del Carlo, P., and Taddeucci, J. (2009). Shifting styles of basaltic explosive activity during the 2002-2003 eruption of Mt. Etna, Italy. *Journal of Volcanology and Geothermal Research,* 180, 110-122.

Annen, C., Blundy, J.D., and Sparks, R.S.J. (2006). The genesis of intermediate and silicic magmas in deep crustal hot zones. *Journal of Petrology,* 47 (3), 505-539.

Applegarth, L.J., Tuffen, H., James, M.R., and Pinkerton, H. (2013). Degassing-driven crystallization in basalts. *Earth-Science Reviews*, 116, 1-16.

Aster, E.M., Wallace, P.J., Moore, L.R., Watkins, J., Gazel, E., and Bodnar, R.J. (2016). Reconstructing CO_2 concentrations in basaltic melt inclusions using Raman analysis of vapor bubbles. *Journal of Volcanology and Geothermal Research*, 323, 148-162.

Beckett, F.M., Burton, M., Mader, H.M., Phillips, J.C., Polacci, M., Rust, A.C., and Witham, F. (2014). Conduit convection driving persistent degassing at basaltic volcanoes. *Journal of Volcanology and Geothermal Research*, 283, 19-35.

Belien, I.L.M.B. (2011). *Gas migration through crystal-rich mafic volcanic systems and applications to Stromboli Volcano, Aeolian Islands, Italy*. University of Oregon, PhD dissertation, 188 p.

Belien, I.B., Cashman, K.V., and Rempel, A.W. (2010). Gas accumulation in particle-rich suspensions and implications for bubble populations in crystal-rich magma. *Earth and Planetary Science Letters*, 297, 133-140.

Bertagnini, A., Métrich, N., Landi, P., and Rosi, M. (2003). Stromboli volcano (Aeolian Archipelago, Italy): An open window on the deep-feeding system of a steady state basaltic volcano. *Journal of Geophysical Research*, 108 (B7), doi:10.1029/2002JB002146.

Blake, S., Self, S., Sharma, K., Sephton, S. (2010). Sulfur release from the Columbia River Basalts and other flood lava eruptions constrained by a model of sulfide saturation. *Earth and Planetary Science Letters*, 299, 328-338.

Bouvet de Maisonneuve, C., Dungan, M.A., Bachmann, O., Burgisser, A. (2012). Insights into shallow magma storage and crystallization at Volcán Llaima (Andean Southern Volcanic Zone, Chile). *Journal of Volcanology and Geothermal Research*, 211-212, 76-91.

Bouvet de Maisonneuve, C. Dungan, M.A., Bachmann, O., Burgisser, A. (2012). Petrological insights into shifts in eruptive styles at Volcán Llaima (Chile). *Journal of Petrology*, 54 (2), 393-420.

Brounce, M.N., Kelley, K.A., Cottrell, E. (2014). The $Fe^{3+}/\sum Fe$ variations in Mariana Arc basalts and primary fO_2 of the mantle wedge. *Journal of Petrology*, 55, 2513-2536.

Bucholz, C.E., Gaetani, G.A., Behn, M.D., Shimizu, N. (2013). Post-entrapment modification of volatiles and oxygen fugacity in olivine-hosted melt inclusions. *Earth and Planetary Science Letters*, 374, 145-155.

Burton, M.R., Mader, H.M., Polacci, M. (2007). The role of gas percolation in quiescent degassing of persistently active basaltic volcanoes. *Earth and Planetary Science Letters*, 264, 46-60.

Cashman, K.V. (2004). *Volatile controls on magma ascent and eruption*. In*:* Sparks, R.S.J. and Hawkesworth C.J. (eds.), *The State of the Planet: Frontiers and Challenges in Geophysics*. American Geophysical Union, doi:10.1029/150GM10.

Castro, J.M., Dingwell, D.B., Nichols, A.R.L., Gardner, J.E. (2005). *New insights on the origin of flow bands in obsidian*. In*:* Manga, M. and Ventura, G. (eds.), *Kinematics and dynamics of lava flows*. Geological Society of America Special Paper, (396), 55-66.

Cembrano, J., and Lara, L. (2008). The link between volcanism and tectonics in the southern volcanic zone of the Chilean Andes: A review. *Tectonophysics*, 471, 96-113.

Cervantes, P., and Wallace, P. (2003). Magma degassing and basaltic eruption styles: a case study of ~ 2000 year BP Xitle volcano in central Mexico. *Journal of Volcanology and Geothermal Research*, 120, 249-270.

Cimarelli, C., Di Traglia, F., and Taddeucci, J. (2010). Basaltic scoria textures from a zoned conduit as precursors to violent Strombolian activity. *Geology*, 38, 439–442. doi:10.1130/G30720.1.

Cimarelli., C., Costa, A., Mueller, S., and Mader, H.M. (2011). Rheology of magmas with bimodal crystal size and shape distributions: Insight from analog experiments. *Geochemistry Geophysics Geosystems*, 12 (7), doi:10.1029/2011GC003606.

Coltelli, M., Del Carlo, P., Pompillio, M., and Vezzoli, L. (2005). Explosive eruption of a picrate: The 3930 BP subplinian eruption of Etna volcano (Italy). *Geophysical Research Letters*, 32 (L23307), doi:10.1029/2005GL024271.

Costa, A., Blake, S., Self, S. (2006). Segregtation processes in vesiculating crystallizing magmas. *Journal of Volcanology and Geothermal Research*, 153, 287-300.

Cottrell, E., Spiegelman, M., and Langmuir, C.H. (2002). Consequences of diffusive reequilibration for the interpretation of melt inclusions. *Geochemistry Geophysics Geosystems*, 3 (5), doi:/10.1029/2001GC000205.

Crabtree, S.M., and Lange, R.A. (2011). Complex phenocryst textures and zoning patterns in andesites and dacites: Evidence of degassing-induced rapid crystallization? *Journal of Petrology*, 52 (1), 3-38.

Danyushevsky, L.V. and Plechov, P. (2011). Petrolog3: Integrated software for modeling crystallization processes. *Geochemistry Geophysics Geosystems*, 12 (7). doi:10. 1029/2011GC003516.

Danyushevsky, L.V., Della-Pasqua, F.N., and Sokolov, S. (2000). Re-equilibration of melt inclusions trapped by magnesian olivine phenocrysts from subduction-related magmas: petrological implications. *Contributions to Mineralogy and Petrology*, 138, 68-83.

Deer, W.A., Howie, R.A., Zussman, J. (1992). *An Introduction to the Rock-Forming Minerals*. Pearson Education, Harlow, England

Del Bello, E., Lane, S.J., James, M.R., Llewellin, E.W., Taddeucci, J., Scarlato, P., and Capponi, A. (2015). Viscous plugging can enhance and modulate explosivity of strombolian eruptions. *Earth and Planetary Science Letters*, 423, 210-218.

Delgado, F., Pritchard, M.E., Ebmeier, S., González, P., and Lara, L. (in preparation). Recent unrest (2002-2015) imaged by space geodesy at the highest risk Chilean volcanoes: Llaima, Villarrica, and Calbuco (Southern Andes). *Journal of Volcanology and Geothermal Research.*

Dixon, J.E. and Stolper, E.M. (1995). An experimental study of water and carbon dioxide solubilities in mid-ocean ridge basaltic liquids. Part II: Applications to degassing. *Journal of Petrology*, 36 (6), 1633-1646.

Dixon, J.E., Stolper, E.M., Holloway, J.R. (1995). An experimental study of water and carbon dioxide solubilities in mid-ocean ridge basaltic liquids. Part I: Calibration and solubility models. *Journal of Petrology*, 36 (6), 1607-1631.

Dungan, M.A., Long, P.E., Rhodes, J.M. (1978). Magma mixing at mid-ocean ridges: evidence from legs 45 and 45-DSDP. *Geophysical Research Letters*, 5, 423-425.

Dzierma, Y. and Wehrmann, H. (2010). Eruption time series statistically examined: probabilities of future eruptions at Villarrica and Llaima Volcanoes, Southern Volcanic Zone, Chile. *Journal of Volcanology and Geothermal Research*, 193, 82–92. doi:10.1016/j.jvolgeores.2010.03.009.

Edmonds, M., Kohn, S.C., Hauri, E.H., Humphreys, M.C.S., and Cassidy, M. (2016). Extensive, water-rich magma reservoir beneath southern Montserrat. *Lithos*, 252-253, 216-233.

Erlund, E.J., Cashman, K.V., Wallace, P.J., Pioli, L., Rosi, M., Johnson, E., Delgado Granados, H. (2011). Compositional evolution of magma from Parícutin Volcano, Mexico: The tephra record. *Journal of Volcanology and Geothermal Research*, 197, 167-187.

Francalanci, L., Tommasini, S., and Conticelli, S. (2004). The volcanic activity of Stromboli in the 1906-1998 AD period: mineralogical, geochemical and isotopic data relevant to the understanding of the plumbing system. *Journal of Volcanology and Geothermal Research*, 131, 179-211.

Ford, C.E., Russell, D.G., Groven, J.A. ,and Fisk, M.R. (1983). Distribution coefficients of Mg^{2+}, Fe^{2+}, Ca^{2+} and Mn^{2+} between olivine and melt. *Journal of Petrology*, 24, 256–265.

Fournier, T.J., Pritchard, M.E., and Riddick, S.N. (2010). Duration, magnitude, and frequency of subaerial volcano deformation events: New results from Latin America using InSAR and a global synthesis. *Geochemistry Geophysics Geosystems*, Q01003, doi:10.1029/2009GC002558.

Gaetani, G.A. O'Leary, J.A., Shimizu, N., Bucholz, C.E., Newville, M. (2012). Rapid reequilibration of H_2O and oxygen fugacity in olivine-hosted melt inclusions. *Geology*, 40, 915-918.

Genereau, K., Valentine, G.A., Moore, G., Hervig, R.L. (2010). Mechanisms for transition in eruptive style at a monogenetic scoria cone revealed by microtextural analyses (Lathrop Wells volcano, Nevada, U.S.A.). *Bulletin of Volcanology*, 72, 593-607.

Global Volcanism Program. (2008). Report on Llaima (Chile). In: Wunderman, R (ed.), *Bulletin of the Global Volcanism Network*, 33:6. Smithsonian Institution. http://dx.doi.org/10.5479/si.GVP.BGVN200806-357110.

Govindaraju, K. (1994). Compilation of working values and sample description for 383 geostandards. *Geostandards Newsletter*, 18, 1-158.

Hammer, J.E. (2008). Experimental studies of the kinetics and energetics of magma crystallization. *Reviews in Mineralogy*, 69, 9-59.

Hantke, G. (1962). Übersicht über die vulkanische Tätigkeit 1957-1959. *Bullitin Volcanologique*, 24 (1), 321-348.

Hayward, C. (2012). High spatial resolution probe microanalysis of tephras and melt inclusions without beam-induced chemical modification. *The Holocene*, 22, 119-125.

Higgins, M.D. (2000). Measurement of crystal size distributions. *American Mineralogist*, 85, 1105–1116.

Higgins, M.D. (2006). *Quantitative Textural Measurements in Igneous and Metamorphic Petrology*. Cambridge University Press, Cambridge, UK.

Higgins, M.D. and Roberge, J. (2003). Crystal size distribution (CSD) of plagioclase and amphibole from Soufriere Hills volcano, Montserrat: evidence for dynamic crystallisation/textural coarsening cycles. *Journal of Petrology*, 44, 1401–1411.

Helo, C., Longprém M-A., Shimizu, N., Clague, D.A., Stix, J. (2011). Explosive eruptions at mid-ocean ridges driven by CO_2-rich magmas. *Nature Geoscience*, 4, 260-263.

Hervig, R.L., Mazdab, F.K., Moore, G., McMillan, P.F. (2003). Analyzing hydrogen (H_2O) in silicate glass by secondary ion mass spectrometry and reflectance Fourier transform infrared spectroscopy. *Developments in Volcanology*, 5, 83-103.

Hickey-Vargas, R.L., Frey, F.A., Gerlach, D.C. (1986). Multiple sources for basaltic arc rocks from the Southern Volcanic Zone of the Andes (34°-41° S): Trace element and isotopic evidence for contributions from subducted oceanic crust, mantle, and continental crust. *Journal of Geophysical Research*, 91 (B6), 5963-5983.

Houghton, B.F. and Gonnermann, H.M. (2008). Basaltic explosive volcanism: Constraints from deposits and models. *Chemie der Erde*, 68, 117-140.

Houghton, B.F., and Wilson, C.J.N. (1989). A vesicularity index for pyroclastic deposits. *Bulletin of Volcanology*, 51, 451–462,

Jacques, G., Hoernle, K., Gill, J., Wehrmann, H., Bindemann, I., Lara, L.E. (2014). Geochemical variations in the Central Southern Volcanic Zone, Chile (38-43 °S): The role of fluids in generating arc magmas. *Chemical Geology*, 371, 27-45.

Jaupart, C. (1998). Gas loss from magmas through conduit walls during eruption. In: Gilbert, J. S. and Sparks, R.S.J. (eds.) *The Physics of Explosive Volcanic Eruptions*. Geological Society, London, Special Publications, 145, 73-90.

Jochum, K.P., Stoll, B., Herwig, K., Willbold, M., Hofmann, A.W., Amini, M., Aarburg, S., Abouchami, W., Hellebrand, E., Mocek, B., Raczek, I., Stracke, A., Alard, O., Bouman, C., Becker, S., Dücking, M., Brätz, H., Klemd, R., de Bruin, D., Canil, D., Cornell, D., de Hoog, C-J., Dalpé, C., Danyushevsky, L., Eisenhauer, A., Gao, Y., Snow, J.E., Groschopf, N., Günther, D., Latkoczy, C., Guillong, M., Hauri, E.H., Höfer, H.E., Lahaye, Y., Horz, K., Jacob, D.E., Kasemann, S.A., Kent, A.J.R., Ludwig, T., Zack, T., Mason, P.R.D., Meixner, A., Rosner, M., Misawa, K., Nash, B.P., Pfänder, J., Premo, W.R., Sun, W.D., Tiepolo, M., Vannucci, R., Vennemann, T., Wayne, D., and Woodhead, J.D. (2006). MPI-DING reference glasses for in situe microanalysis: New reference values for element concentrations and isotope ratios. *Geochemistry Geophysics Geosystems*, 7 (2), doi:10.1029/2005GC001060.

Johnson, E.R., Wallace, P.J., Cashman, K.V., Delgado Granados, H., Kent, A.J.R. (2008). Magmatic volatile contents and degassing-induced crystallization at Volcán Jorullo, Mexico: Implications for melt evolution and the plumbing systems of monogenetic volcanoes. *Earth and Planetary Science Letters*, 269, 478-487.

Johnson, E.R., Wallace, P.J., Cashman, K.V., Delgado Granados, H. (2010). Degassing of volatiles (H_2O, CO_2, S, Cl) during ascent, crystallization, and eruptions at mafic monogenetic volcanoes in central Mexico. *Journal of Volcanology and Geothermal Research*, 197, 225-238.

Kazahaya, K., Shinohara, H., Saito, G. (1994). Excessive degassing of Izu-Oshima volcano: Magma convection in a conduit. *Bulletin of Volcanology*, 56, 207-216.

Kelley, K.A., and Cottrell, E. (2009). Water and the oxidation state of subduction zone magmas. *Science*, 325, 605-607

Kelley, K.A. and Cottrell, E. (2012). The influence of magmatic differentiation on the oxidation state of Fe in a basaltic arc magma. *Earth and Planetary Science Letters*, 329-330, 109-121.

Kelley, K.A., Plank, T., Ludden, J., Staudigel, H. (2003). Composition of altered oceanic crust at ODP Sites 801 and 1149. *Geochemistry Geophysics Geosystems*, 4 (6), 8910. doi:10.1029/2002GC000435.

Kent, A.J.R. (2008). Melt inclusions in basaltic and related volcanic rocks. *Reviews in Mineralogy*, 69, 273-331.

Kress, V.C. and Carmichael I.S.E. (1991). The compressibility of silicate liquids containing Fe_2O_3 and the effect of composition, temperature, oxygen fugacity and pressure on their redox states. *Contributions to Mineralogy and Petrology*, 108, 82-92.

Landi, P., Métrich, N., Bertagnini, A., and Rosi, M. (2004). Dynamics of magma mixing and degassing recorded in plagioclase at Stromboli (Aeolian Archipelago, Italy). Contributions to Mineralogy and Petrology, 147, 213-227.

Lange, R.A., Frey, H.M., and Hector, J. (2009). A thermodynamic model for the plagioclase-liquid hygrometer/thermometer. *American Mineralogist*, 94, 494-506.

Laiolo, M. and Cigolini, C. (2006). Mafic and ultramafic xenoliths in San Bartolo lava field: New insights on the ascent and storage of Stromboli magmas. *Bulletin of Volcanology*, 68, 653-670.

Lautze, N.C. and Houghton, B.F. (2007). Linking variable explosion style and magma textures during 2002 at Stromboli volcano, Italy. *Bulletin of Volcanology*, 69, 445-460.

Lloyd, A.S., Plank, T., Ruprecht, P., Hauri, E.H., Rose. W. (2013). Volatile loss from melt inclusions in pyroclasts of differing sizes. *Contributions to Mineralogy and Petrology*, 165 (1), 129-153.

Lofgren, G. (1974). An experimental study of plagioclase crystal morphology: Isothermal crystallization. *American Journal of Science*, 274, 243– 273.

Lucassen, F., Trumbull, R., Franz, G., Creixell, C., Vásquez, P., Romer, R.L., and Figueroa, O. (2004). Distinguishing crustal recycling and juvenile additions at active continental margins: the Paleozoic to recent composition evolution of the Chilean Pacific margin (36-41 °S). *Journal of South American Earth Sciences*, 17, 103-119.

Luhr, J.F. (2001). Glass inclusions and melt volatile contents at Parícutin Volcano, Mexico. *Contributions to Mineralogy and Petrology*, 142, 261-283.

Lytle, M.L., Kelley, K.A., Hauri, E.H., Gill, J.B., Papia, D., Arculus, R.J. (2012). Tracing mantle sources and Samoan influence in the northwestern Lau back-arc basin. *Geochemistry Geophysics Geosystems*, 13 (10), Q10019. doi:10.1029/2012GC004233.

Mandeville, C.W., Sasaki, A., Saito, G., Faure, K., King, R., and Hauri, E. (1998). Open-system degassing of sulfur from Krakatau 1883 magma. *Earth and Planetary Science Letters*, 160, 709-722.

Mangan, M.T. and Cashman, K.V. (1996). The structure of basaltic scoria and reticulate and inferences for vesiculation, foam formation, and fragmentation in lava fountains. *Journal of Volcanology and Geothermal Research*, 73, 1-18.

Marsh, B.D. On the interpretation of crystal size distributions in magmatic systems. *Journal of Petrology*, 39 (4), 553-599.

Menand, T. and Phillips, J.C. (2007). Gas segregation in dykes and sills. *Journal of Volcanology and Geothermal Research*, 159, 393-408.

Métrich, N. and Wallace, P.J. (2008). Volatile abundances in basaltic magmas and their degassing paths tracked by melt inclusions. *Reviews in Mineralogy*, 69, 363-402.

Métrich, N., Bertagnini, A., Landi, P., Rosi, M. (2001). Crystallization driven by decompression and water loss at Stromboli Volcano (Aeolian Island, Italy). *Journal of Petrology*, 42 (8), 1471-1490.

Métrich, N., Bertagnini, A., Di Muro, A. (2010). Conditions of magma storage, degassing and ascent at Stromboli: New Insights into the volcano plumbing system with inferences on the eruptive dynamics. *Journal of Petrology*, 51 (3), 603-626.

Moitra, P., Gonnermann, H.M., Houghton, B.F., and Giachetti, T. (2013). Relating vesicle shape in pyroclasts to eruption styles. *Bulletin of Volcanology*, 75, 691, doi:10.1007/s00445-013-0691-8.

Moore, G. (2008). Interpreting H_2O and CO_2 contents in melt inclusions: Constraints from solubility experiments and modeling. *Reviews in Mineralogy*, 69, 333-361.

Moreno, H. and Fuentealba, G. (1994). The May 17-19 1994 Llaima Volcano eruption, Southern Andes (38°42’ S 71°44’W). *Revista Geológica de Chile*, 21 (1), 167-171.

Morgan, D.J. and Jerram, D.A. (2006). On estimating crystal shape for crystal size distribution analysis. *Journal of Volcanology and Geothermal Research*, 154, 1-7.

Naranjo S., J.A., Moreno R., H. (2005). *Geologíca del Volcan Llaima, Regíon de la Araucanía*. Carta Geológica de Chile, Serie Geológica Básica. Servicio Nacional de Geología y Minería, Santiago, 88.

Neave, D.A., Maclennan, J., Edmonds, M., and Thordarson, T. (2014). Melt mixing causes negative correlation of trace element enrichment and CO_2 content prior to an Icelandic eruption. *Earth and Planetary Science Letters*, 400, 272-283.

Newman, S. and Lowenstern, J.B. (2002). VolatileCalc: A silicate melt-H_2O-CO_2 solution model written in Visual Basic for Excel. *Computers and Geosciences*, 28, 597-604.

Newman, S., Stolper, E., Stern, R. (2000). H_2O and CO_2 in magmas from the Mariana arc and back arc systems. *Geochemistry Geophysics Geosystems*, 1 (1), doi:10.1029/1999GC000027.

Nichols, A.R.L. and Wysoczanski, R.J. (2007). Using micro-FTIR spectroscopy to measure volatile contents in small and unexposed inclusions hosted in olivine crystals. *Chemical Geology*, 242, 371-384.

Oppenheimer, C., Moretti, R., Kyle, P.R., Eschenbacher, A., Lowenstern, J.B., Hervig, R.L., and Dunbar, N.W. (2011). Mantle to surface degassing of alkali magmas at Erebus volcano, Antarctica. *Earth and Planetary Science Letters*, 306, 261-271.

Palma, J.L., Blake, S., Calder, E.S. (2011). Constraints on the rates of degassing and convection in basaltic open-vent volcanoes. *Geochemistry Geophysics Geosystems*, 12 (11), Q11006. doi:10.1029/2011GC003715.

Pansino, S. (2012). *Experimental analysis of bubble-driven mixing in a volcanic conduit and how it affects lava lake sustainability*. University at Buffalo, MS thesis, 59 p.

Papale, P., Moretti, R., Barbato, D. (2006). The compositional dependence of the saturation surface of H_2O+CO_2 fluids in silicate melts. *Chemical Geology*, 229, 78-95.

Parfitt, E.A. and Wilson, L. (1995). Explosive volcanic eruptions – IX. The transition between Hawaiian-style lava fountaining and Strombolian explosive activity. *Geophysical Journal International*, 121, 226-232.

Petit-Breuilh, M.E. (2006). *La Historia Eruptiva de los volcanes Hispanoamericanos (Siglos XVI al XX)*. Huelva, Spain, Sevicio de Pulicaciones del Cabildo Insular de Lanzarote.

Pioli, L., Azzopardi, B.J., and Cashman, K.V. (2009). Controls on the explosivity of scoria cone eruptions: Magma segregation at conduit junctions. *Journal of Volcanology and Geothermal Research*, 186, 407-415.

Pioli, L., Erlund, E., Johnson, E., Cashman, K., Wallace, P., Rosi, M., and Delgado Granados, H. (2008). Explosive dynamics of violent Strombolian eruptions: The eruption of Parícutin Volcano 1943–1952 (Mexico). *Earth and Planetary Science Letters*, 271, 359–368. doi:10.1016/j.epsl.2008.04.026

Pistone, M., Arzilli, F., Dobson, K.J., Cordonnier, B., Reusser, E., Ulmer, P., Marone, F., Whittington, A.G., Mancini, L., Fife, J.L., and Blundy, J.D. (2015). Gas-driven filter pressing in magmas: Insights into in-situ melt segregation from crystal mushes. *Geology*, doi:10.1130/G36766.1.

Polacci, M., Corsaro, R.A., and Andronico, D. (2006). Coupled textural and compositional characterization of basaltic scoria: Insights into the transition from Strombolian to fire fountain activity at Mount Etna, Italy. *Geology*, 34 (3), 201-204.

Portnyagin, M., Almeev, R., Matveev, S., Holtz, F. (2008). Experimental evidence for rapid water exchange between melt inclusions in olivine and host magma. *Earth and Planetary Science Letters*, 272, 541-552.

Preece, K., Gertisser, R., Barclay, J., Charbonnier, S.J., Komorowski, J-C., Herd, R.A. (2016). Transitions between explosive and effusive phases during the cataclysmic 2010 eruption of Merapi volcano, Java, Indonesia. *Bulletin of Volcanology*, 78, doi:/10.1007/s00445-016-1046-z.

Putirka, K.D. (2008). Thermometers and barometers for volcanic systems. *Reviews in Mineralogy*, 69, 61-120.

Putirka, K.D., Perfit, M., Ryerson, F.J., Jackson, M.G. (2007). Ambient and excess mantle temperatures, olivine thermometry, and active vs. passive upwelling. *Chemical Geology*, 241, 177-206.

Reichen, L.E. and Fahey, J.J. (1962). An improved method for the determination of FeO in rocks and minerals including garnet. *United States Geological Survey Bulletin,* 1144(B), 1-5.

Reubi, O., Bourdon, B., Dungan, M.A., Koorneef, J.M., Sellés, D., Langmuir, C.H., Aciego, S. (2011). Assimilation of the plutonic roots of the Andean arc controls variations in U-series disequilibria at Volcan Llaima, Chile. *Earth and Planetary Science Letters*, 303, 37-47.

Remy, D., Chen, Y., Froger, J.L, Bonvalot, S., Cordoba, L., and Fustos, J. (2015). Revised interpretation of recent InSAR signals observed at Llaima volcano (Chile). *Geophysical Research Letters*, doi:10.1002/2015GL063872.

Rhodes, J.M., Dungan, M.A., Blanchard, D.P., and Long, P.E. (1979). Magma mixing at mid-ocean ridges: evidence from basalts drilled near 22 °N on the mid-Atlantic ridge. *Tectonophysics*, 55, 35-61.

Roeder, P.L. and Emslie, R.F. (1970). Olivine-liquid equilibrium. *Contributions to Mineralogy and Petrology*, 29, 275-289.

Roggensack, K., Hervig, R.L., McKnight, S.B., Williams, S.N. (1997). Explosive basaltic volcanism from Cerro Negro volcano: Influences of volatiles on eruptive style. *Science*, 277, 1639-1642.

Rose, W.I., Palma, J.L., Delgado Granados, H., and Varley, N. (2013). Open-vent volcanism and related hazards: Overview. *Geological Society of America Special Papers*, 498, vii-xiii, doi:10.1130/2013.2498(00).

Rosi, M., Bertagnini, A., Landi. (2000). Onset of the persistent activity at Stromboli Volcano (Italy). *Bulletin of Volcanology*, 62, 294-300.

Rosi, M., Pistolesi, M., Bertagnini, A., Landi, P., Pompilio, M., and Di Roberto, A. (2013). Stromboli volcano, Aeolian Islands (Italy): present eruptive activity and hazards, In: Lucchi, F., Peccerillo, A., Keller, T., and Tranne, C.A. (eds.), *The Aeolian Island Volcanoes*. Geological Society of London Memoirs, 37, 473-490.

Ruth, D.C.S. (2014) *Physical and geochemical systematics of the 2008 violent Strombolian eruption of Llaima volcano, Chile*. University at Buffalo, PhD dissertation, 203 p.

Ruth, D.C.S. and Calder, E.S. (2014). Plate tephra: Preserved bubble walls from large slug bursts during violent Strombolian eruptions. *Geology*, 42, 11-14, doi: 10.1130/G34859.1

Sable, J.E., Houghton, B.F., Del Carlo, P., and Coltelli, M. (2006). Changing conditions of magma ascent and fragmentation during the Etna 122 BC basaltic Plinian eruption: Evidence from clast microtextures. *Journal of Volcanology and Geothermal Research, 158*, 333-354.

Schonwalder-Angel, D.A. (2015). *The emplacement of satellite scoria cones at Llaima Volcanic System, Chile: The interaction between magmatic overpressure and the local tectonics*. University at Buffalo, PhD dissertation, 280 p.

Sisson, T.W. and Bacon, C.R. (1999). Gas-driven filter pressing in magmas. *Geology*, 27 (6), 613-616.

Stevenson, D.S. and Blake, S. (1998). Modelling the dynamics and thermodynamics of volcanic degassing. *Bulletin of Volcanology*, 60, 307-317.

Stolper, E.M. (1982a). Water in silicate glasses: An infrared spectroscopic study. *Contributions to Mineralogy and Petrology*, 81, 1-13.

Stolper, E.M. (1982b). The speciation of water in silicate melts. *Geochimica and Cosmochimica Acta*, 46, 2609-2620.

Streck, M.J. (2008). Mineral textures and zoning as evidence for open system processes. *Reviews in Mineralogy*, 69, 623-649.

Streck, M.J., Dungan, M.A., Malavassi, E., Reagan, M.K., and Bussy, F. (2002). The role of basalt replenishment in the generation of basaltic andesites of the ongoing activity at Arenal volcano, Costa Rica: evidence from clinopyroxene and spinel. *Bulletin of Volcanology*, 64, 316-327.

Sun, S.-s. and McDonough, W.F. (1989). Chemical and isotopic systematics of ocean basalts: implications for mantle compositions and processes. *Geological Society, London, Special Publication*, 42, 313-345.

Thomas, N., Tait, S., Koyaguchi, T. (1993). Mixing of stratified liquids by the motion of gas bubbles: application to magma mixing. *Earth and Planetary Science Letters*, 115, 161-175.

Toplis, M.J. and Carroll, M.R. (1995). An experimental study of the influence of oxygen fugacity on Fe-Ti oxide stability, phase relations, and mineral-melt equilibria in ferro-basaltic systems. *Journal of Petrology*, 36 (5), 1137-1170.

Tran, A., Rudolph, M.L., and Manga, M. (2015). Bubble mobility in mud and magmatic volcanoes. *Journal of Volcanology and Geothermal Research*, 294, 11-24.

Valentine, G.A. and Gregg, T.K.P. (2008). Continental basaltic volcanoes – Processes and problems. *Journal of Volcanology and Geothermal Research*, 177, 857-873.

Vergniolle, S. and Jaupart, C. (1990). Dynamics of degassing at Kilauea Volcano, Hawaii. *Journal of Geophysical Research*, 95 (B3), 2793-2809.

Vinet, N. and Higgins, M.D. (2010). Magma solidification processes beneath Kilauea volcano, Hawaii: A quantitative textural and geochemical study of the 1969-1974 Mauna Ulu lavas. *Journal of Petrology*, 51 (6), 1297-1332.

Voight, B., Widiwijayanti, C., Mattioli, G., Elsworth, D., Hidayat, D., and Strutt, M. (2010). Magma-sponge hypothesis and stratovolcanoes: Case for a compressible reservoir and quasi-steady deep influx at Soufrière Hills Volcano, Montserrat. *Geophysical Research Letters*, 37 (L00E05), doi:10.1029/2009GL041732.

Wallace, P.J., Kamenetsky, V.S., and Cervantes, P. (2015). Melt inclusion CO_2 contents, pressures of olivine crystallization, and the problem of shrinkage bubbles. *American Mineralogist*, 100, 787-794.

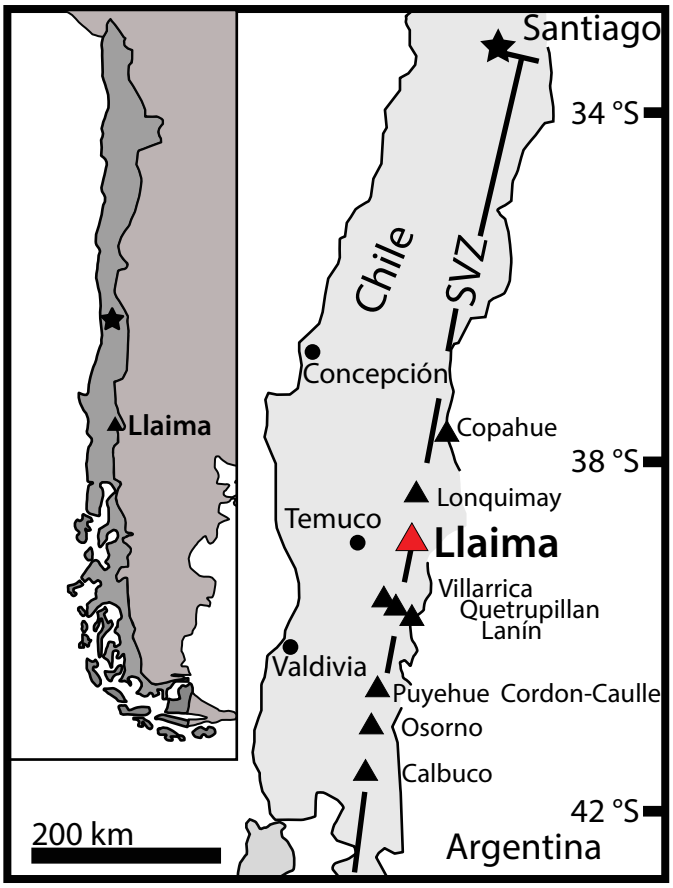

Figure 1. Location map of Llaima within the Southern Volcanic Zone of the Chilean Andes (33-46 °S). Shown for reference are the locations of select nearby volcanic systems, from north to south: Copahue, Lonquimay, Villarrica, Quetrupillan, Lanín, Puyehue Cordon-Caulle, Osorno, and Calbuco.

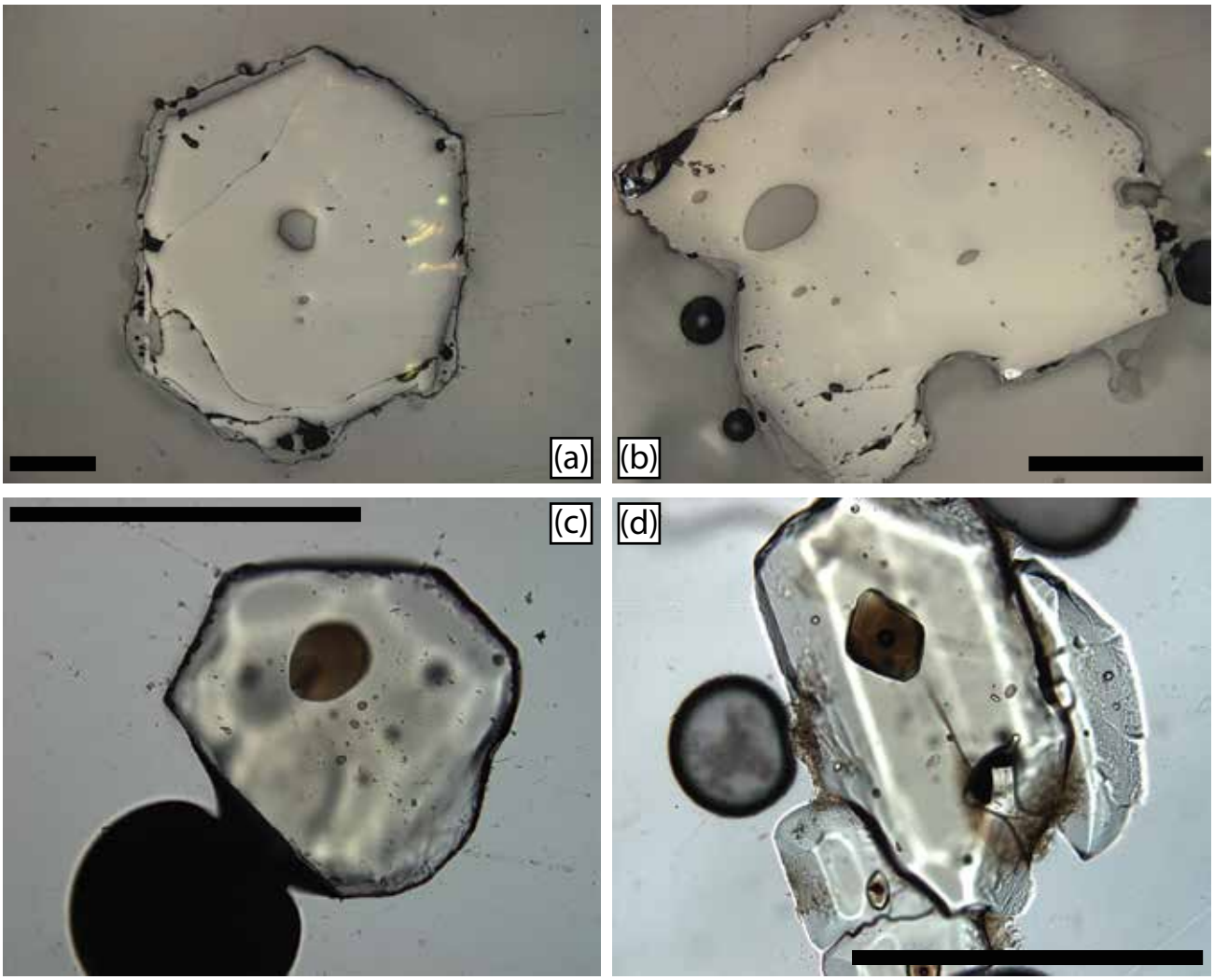

Figure 2. A range of different olivine and melt inclusion morphologies observed in the tephra samples. (A) and (b) are reflected light images whereas (c) and (d) ar e transmitted light images. All scale bars are 500 μm.

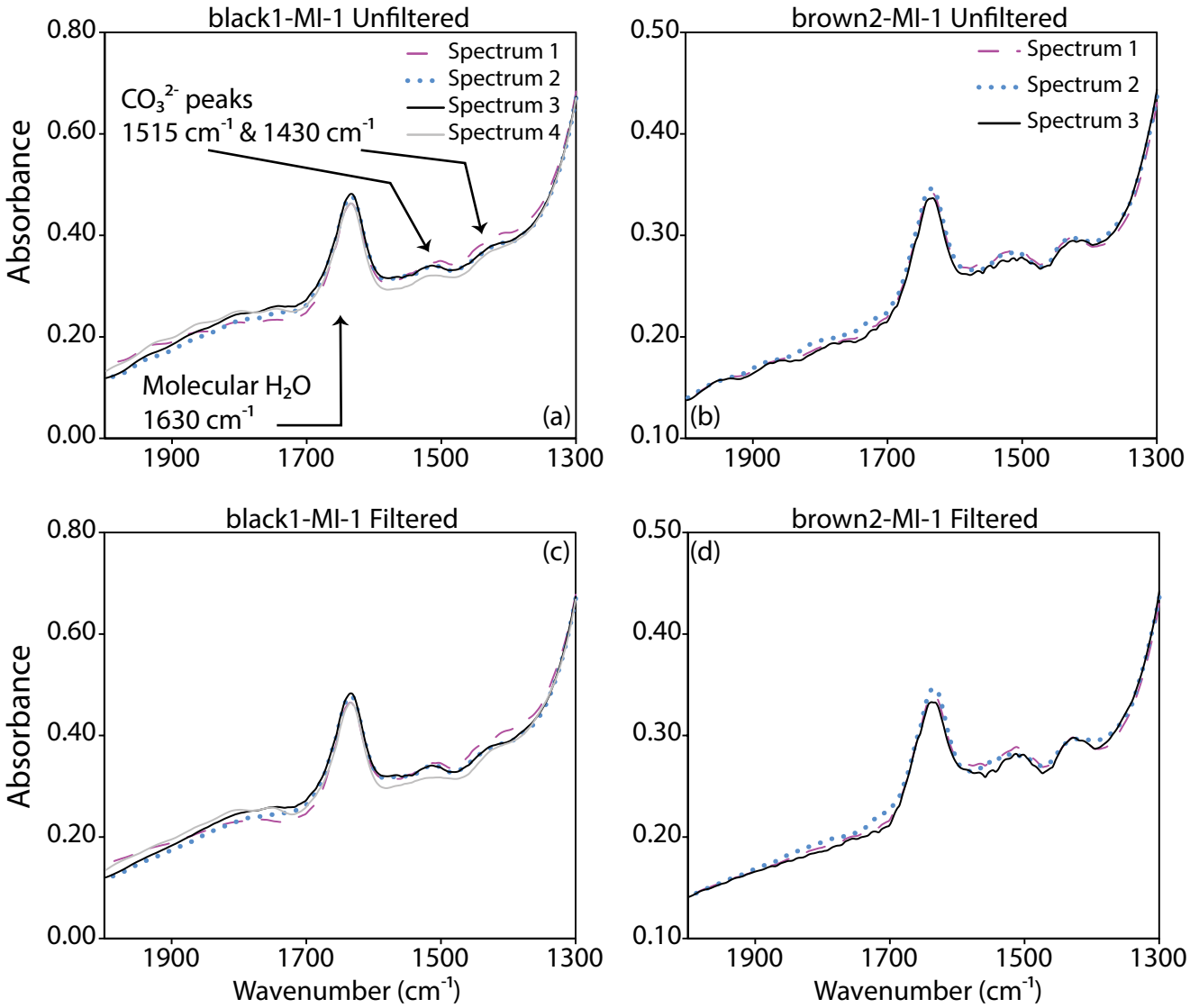

Figure 3. FTIR spectra showing the presence of fringes and the CO32- peaks. Panels (a) and (b) are unfiltered data whereas panels (c) and (d) show the fringes-filtered spectra. There was less than 5% difference between the raw and filtered spectra, indicating that the fringes did not affect the CO32- signal.

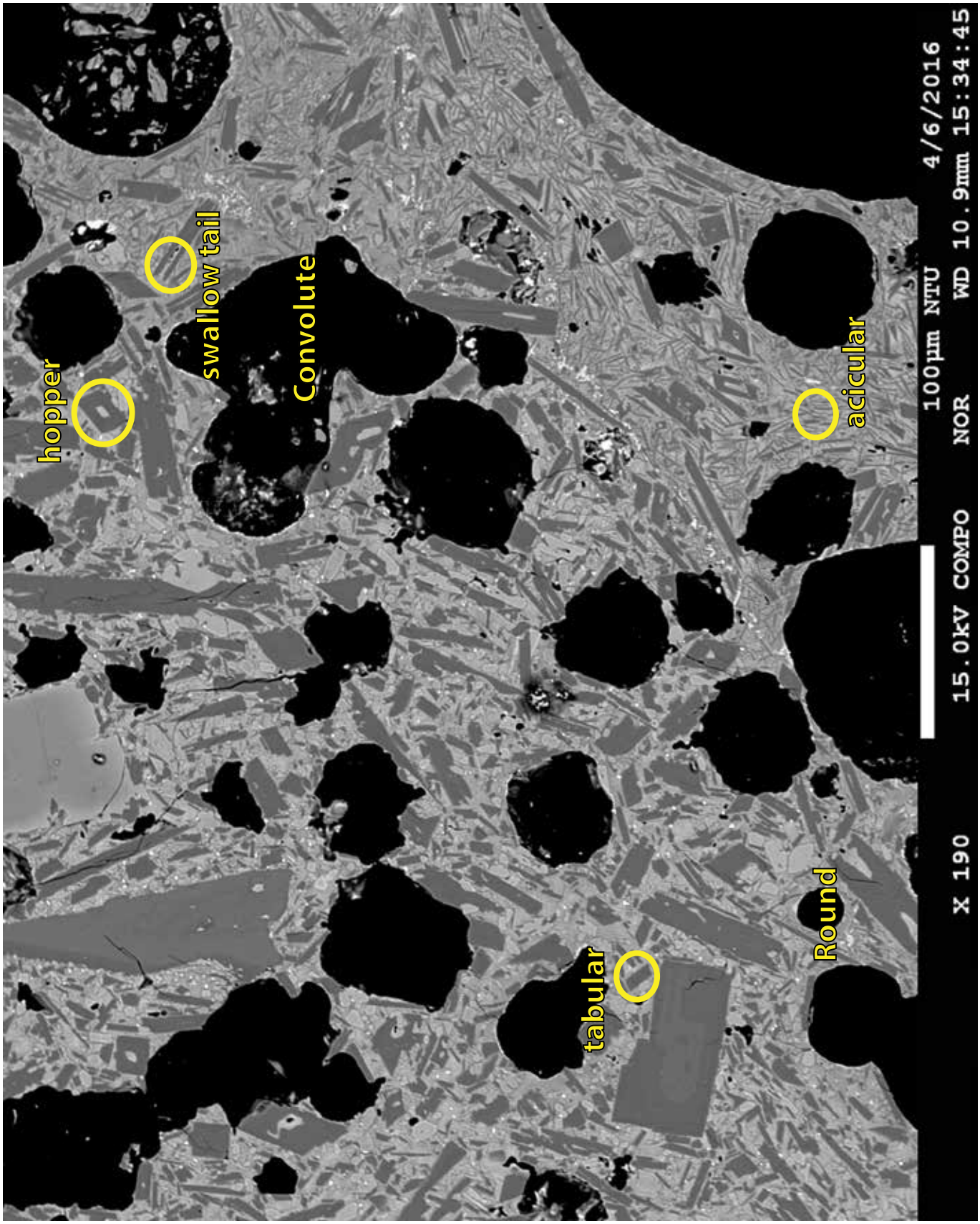

Figure 4. An example backscattered electron image of black scoria, highlighting specific plagioclase and vesicle textural features discussed in this study. With respect to plagioclase, we show hopper, swallow tail, tabular, and acicular morphologies. We highlight round and convolute vesicles.

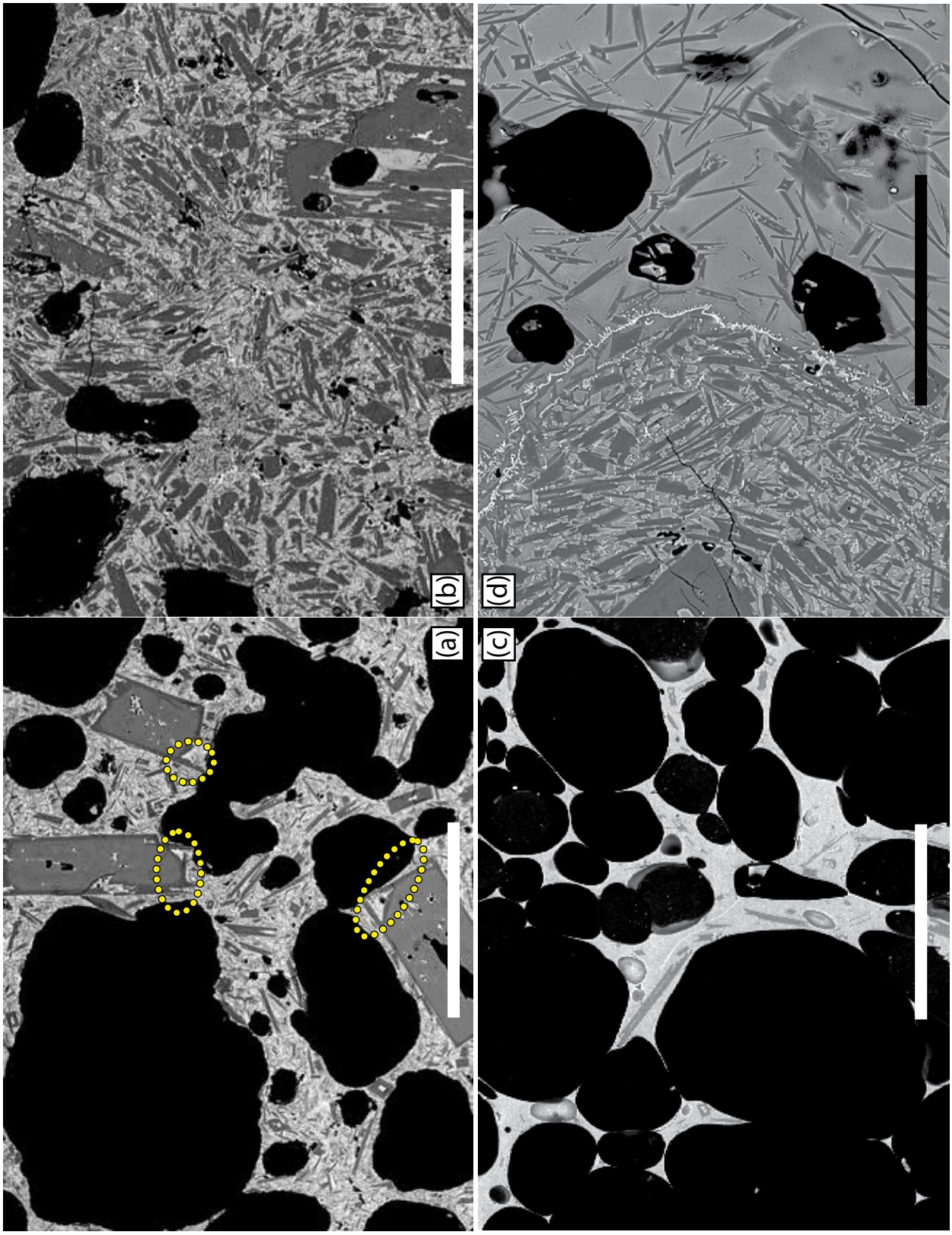

Figure 5. Backscattered electron images of the textural features of black and brown scoria. a) and b) The different microlite textures found in black scoria. In (a) there are abundant acicular plagioclase microlites (dark grey colour) alongside microphenocrysts and phenocrysts. Also note the circled plagioclase phenocrysts in showing the skeletal growths. In (b) the plagioclase microlites are dominantly tabular in morphology. c) The textural features of brown scoria, which show less abundant acicular microlites and abundant vesicles. d) The distinct boundary between two textural domains found in brown scoria. The boundary is highlighted by the spinel with cruciform morphology, suggesting rapid growth. The scale bar is 100 μm.

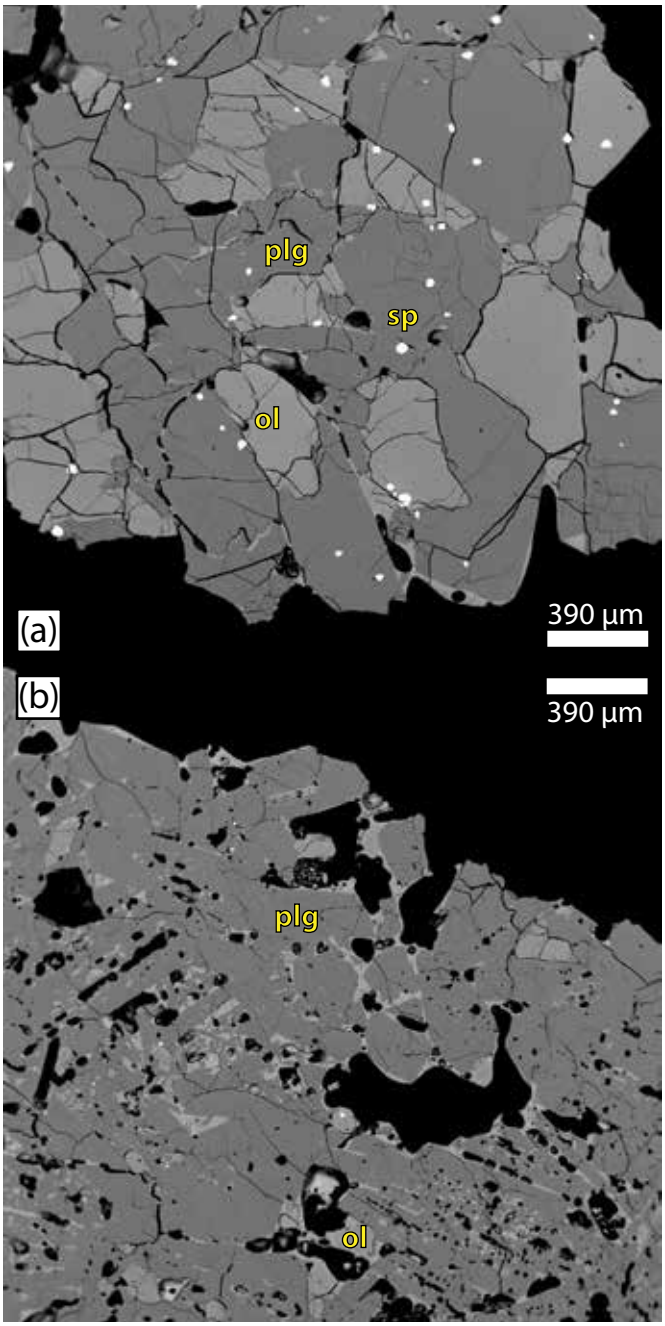

Figure 6. Backscattered electron images of plagioclase-olivine glomerocrysts. The bright phase is spinel, the medium gray phase is olivine, and the dark phase is plagioclase. a) Cr-spinel troctolite glomerocryst in equilibrium with olivine and spinel. Note there are a few vesicles in the surrounding matrix glass. b) Cr-spinel-free troctolite glomerocryst with significantly less olivine and no spinel present.

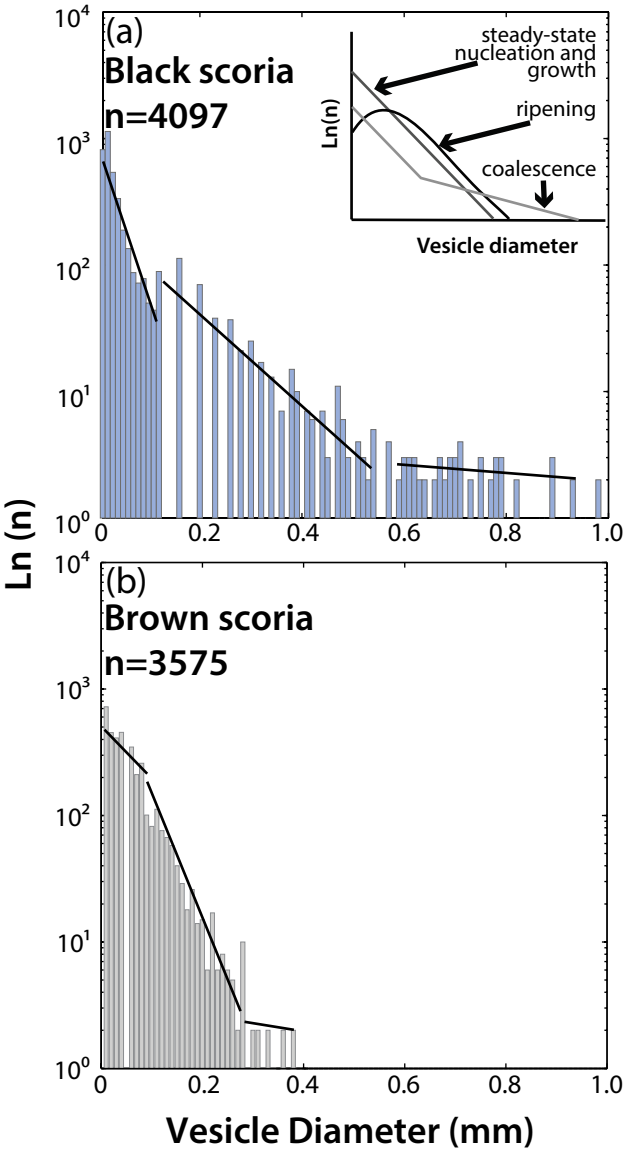

Figure 7. Vesicle size distribution histograms for a) black versus b) brown scoria. Inset figure shows interpretative models of different vesicle size histograms (after Mangan and Cashman, 1996). The lines on the histograms denote the approximate slope of each section. Note small plateau in the small vesicle sizes in the brown scoria, which are indicative of vesicle ripening (Mangan and Cashman, 1996). The black scoria exhibit two linear segments which suggests coalescence and residence.

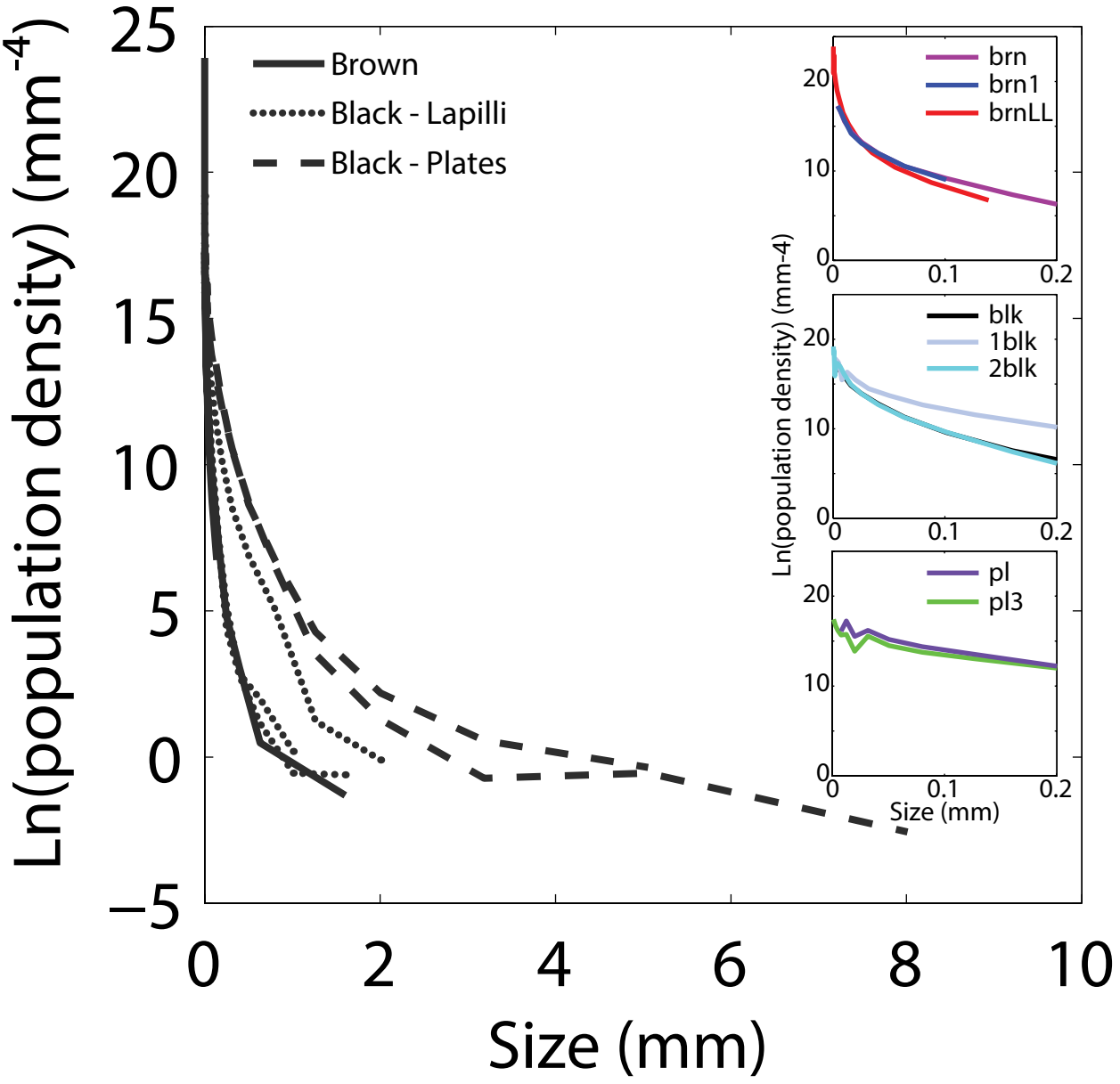

Figure 8. Crystal size distributions for the tephra erupted during the explosive phase. The insets show the breakdown by tephra type and sample. Note the decrease in slope from brown to black scoria to plates. Also note the decrease in y-intercept from brown to black scoria to plates.

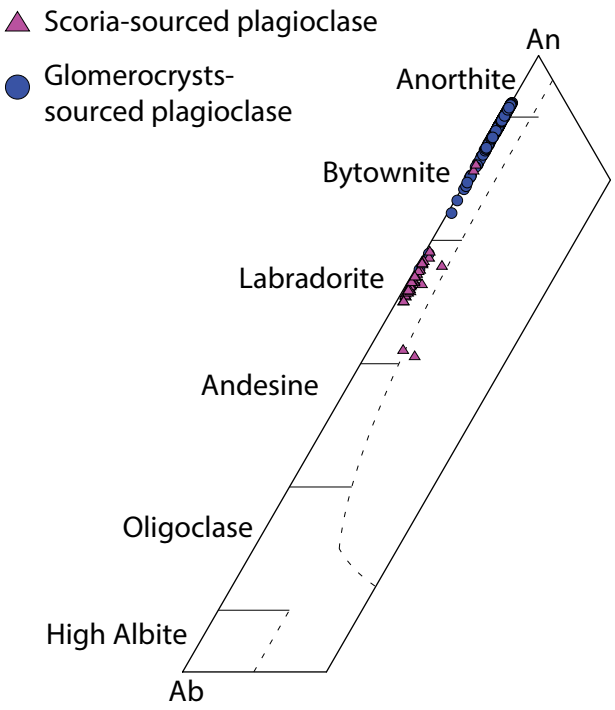

Figure 9. Modified plagioclase ternary diagram following disordered feldspar classification scheme of Deer et al. (1992). The triangles denote scoria-sourced microphenocryst plagioclase whereas the circles are plagioclases found in the glomerocrysts.

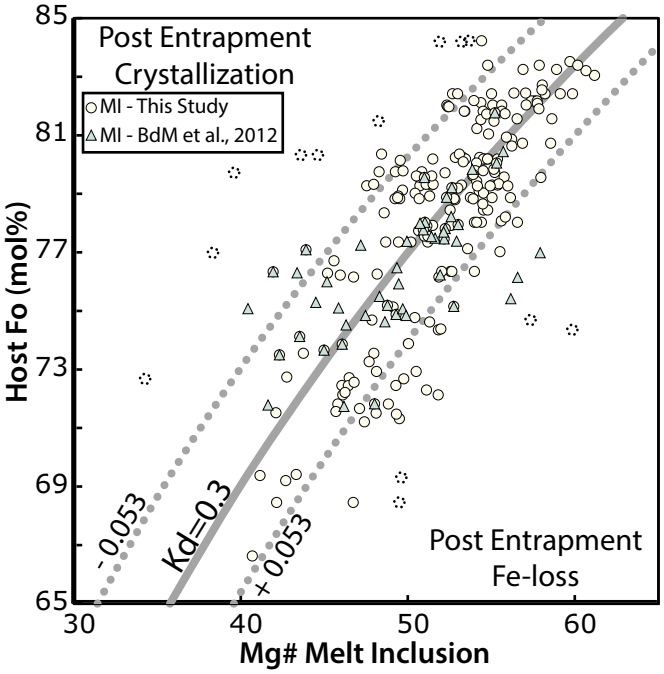

Figure 10. Rhodes diagram of Fo (mol%) of the host olivine and Mg# of the melt inclusion after Dungan et al., 1978; Rhodes et al., 1979). Samples are plotted assuming NNO, and Fe2O3 is 20% of the total Fe (Cervantes and Wallace, 2003). Those data in the top left experience post entrapment crystallization. Those data in the lower right experienced Fe-loss. The bold curve shows equilibrium which equates to Kd=0.3. The dotted lines are acceptable deviations from equilibrium (Putirka, 2008). The circles are melt inclusion analyses from this study whereas the triangles are analyses from the literature (Bouvet de Maisonneuve et al., 2012a). The dotted circles represent samples that were subsequently eliminated for further study due to likely post-entrapment modifications.

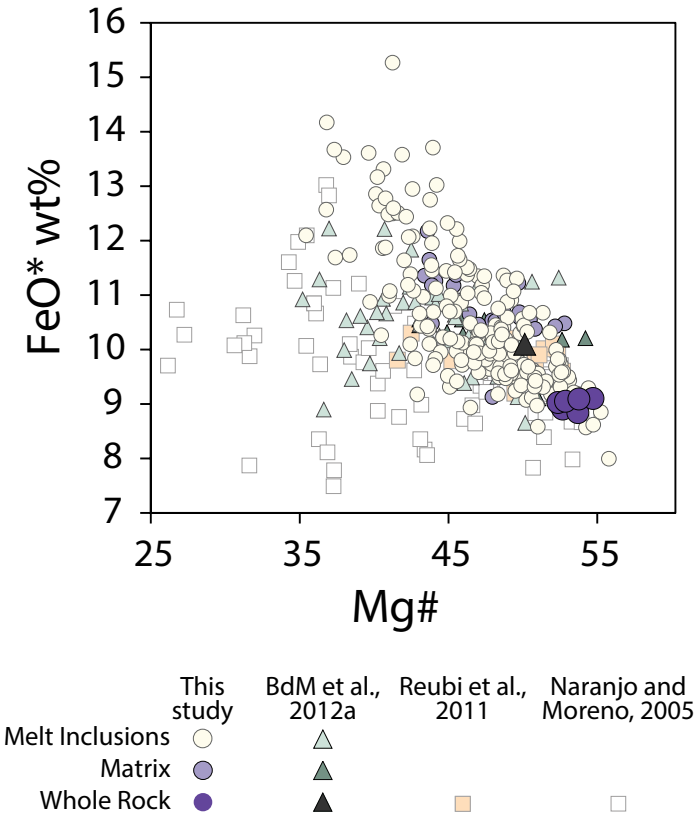

Figure 11. FeO* (total from EMPA) versus the Mg# of the melt inclusion. Also plotted are the matrix glass, and whole rock analyses from this study, Bouvet de Maisonneuve et al. (2012a) (abbreviated as BdM et al. 2012a), Reubi et al. (2011), and Naranjo and Moreno (2005). If the melt inclusions plot along the same trend for the whole rock values then Fe-loss can be considered minimal.

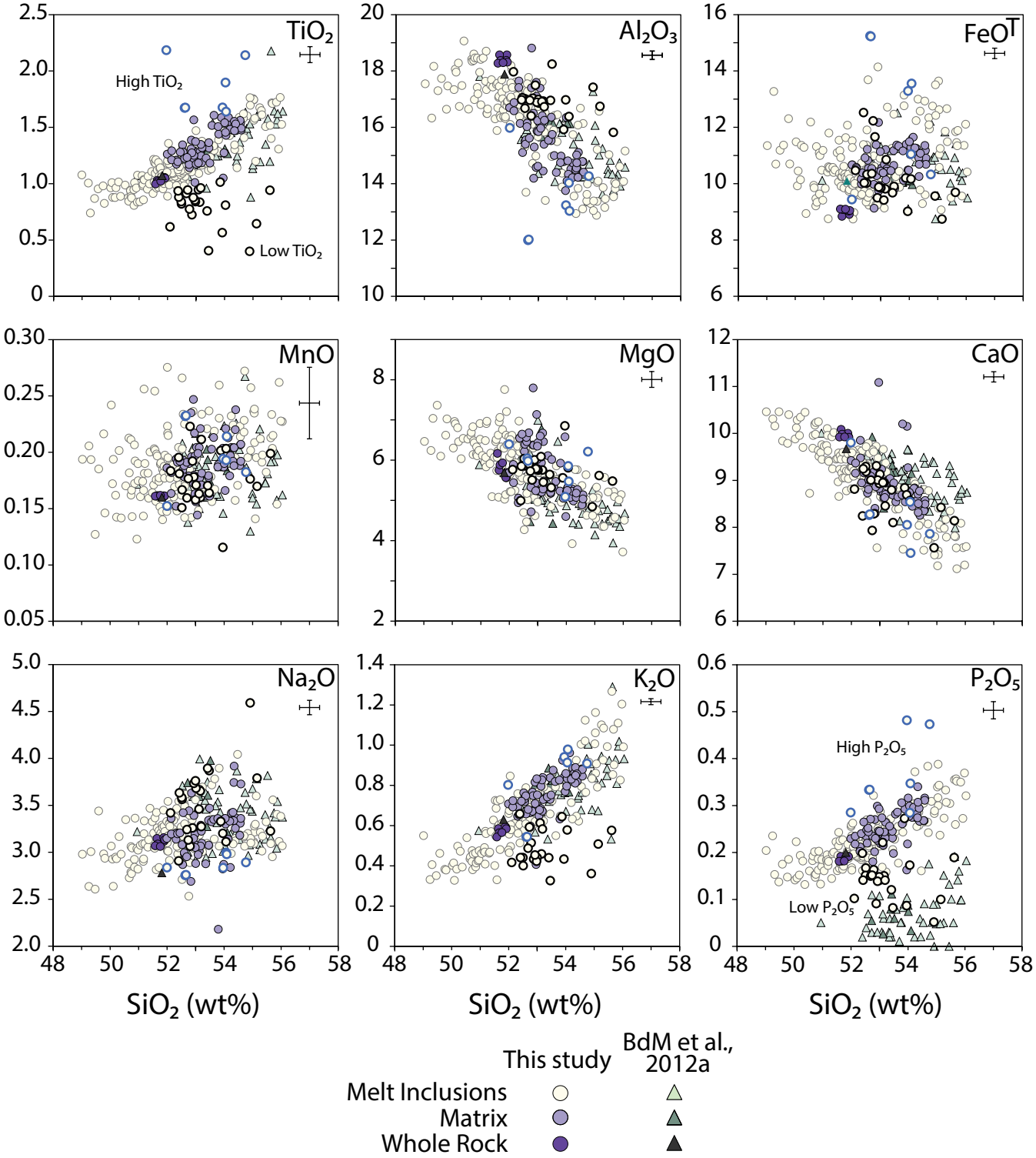

Figure 12. SiO2 diagrams showing the chemical range of the melt inclusions, matrix glass, and whole rock analyses. Samples from Bouvet de Maisonneuve et al. (2012a) are shown for comparison (triangles – same color scheme for whole rock, matrix glass, and melt inclusions). The crosses in the upper right corner represent the average standard deviation of the analyses. CaO, MgO, Al2O3 show negative correlations with SiO2, which is consistent with plagioclase and olivine crystallization. K2O, Na2O, P2O5, TiO2 show incompatible behavior. FeOT and MnO do not show any trends. All values are in wt%. Symbols with dark bold outlines highlight the low TiO2 and P2O5 samples whereas symbols with the lighter bold outlines denote samples with high TiO2 and P2O5.

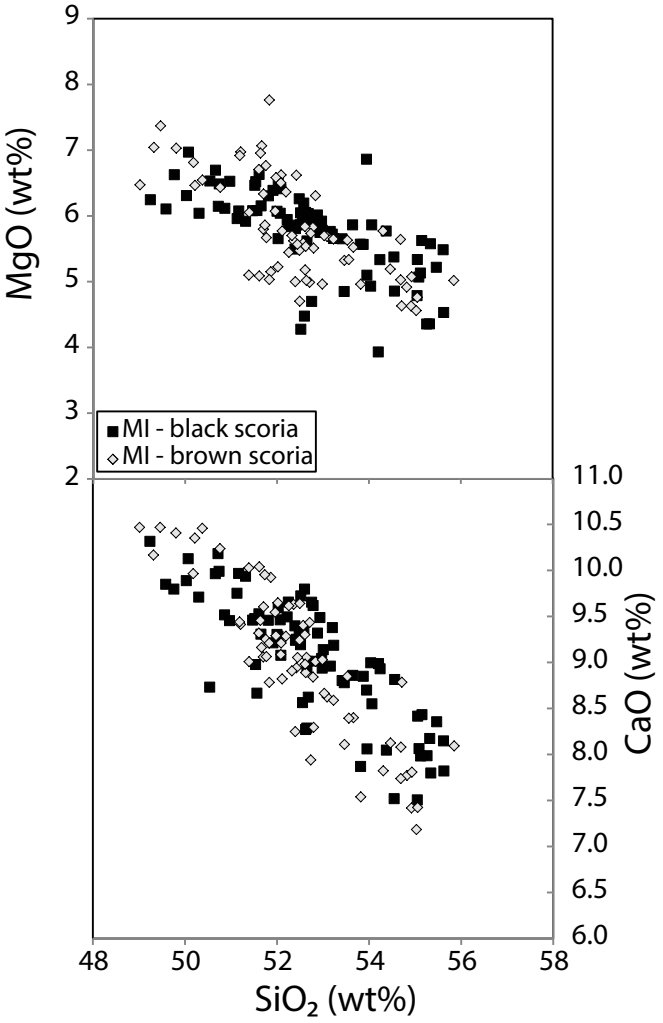

Figure 13. A comparison of melt inclusions sourced from the black and brown scoria to determine if there were distinct populations. The overlap of these data sets indicates that their respective melt inclusions are indistinguishable in terms of major elements (MgO and CaO).

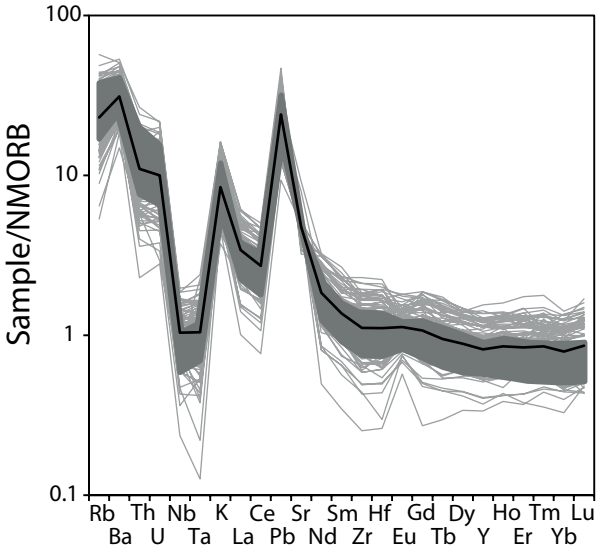

Figure 14. Multielement plot of trace elements in all analyzed melt inclusions with the average value shown in black. The dark gray field represents whole rock trace element data from Llaima Holocene tephra from Jacques et al. (2014). Note the subduction zone signature with the enriched large-ion lithophile elements, and light rare earth elements with respect to the heavy rare earth elements. Also note the range of Nb-Ta anomalies. Normalized values are from Sun and McDonough, 1989.

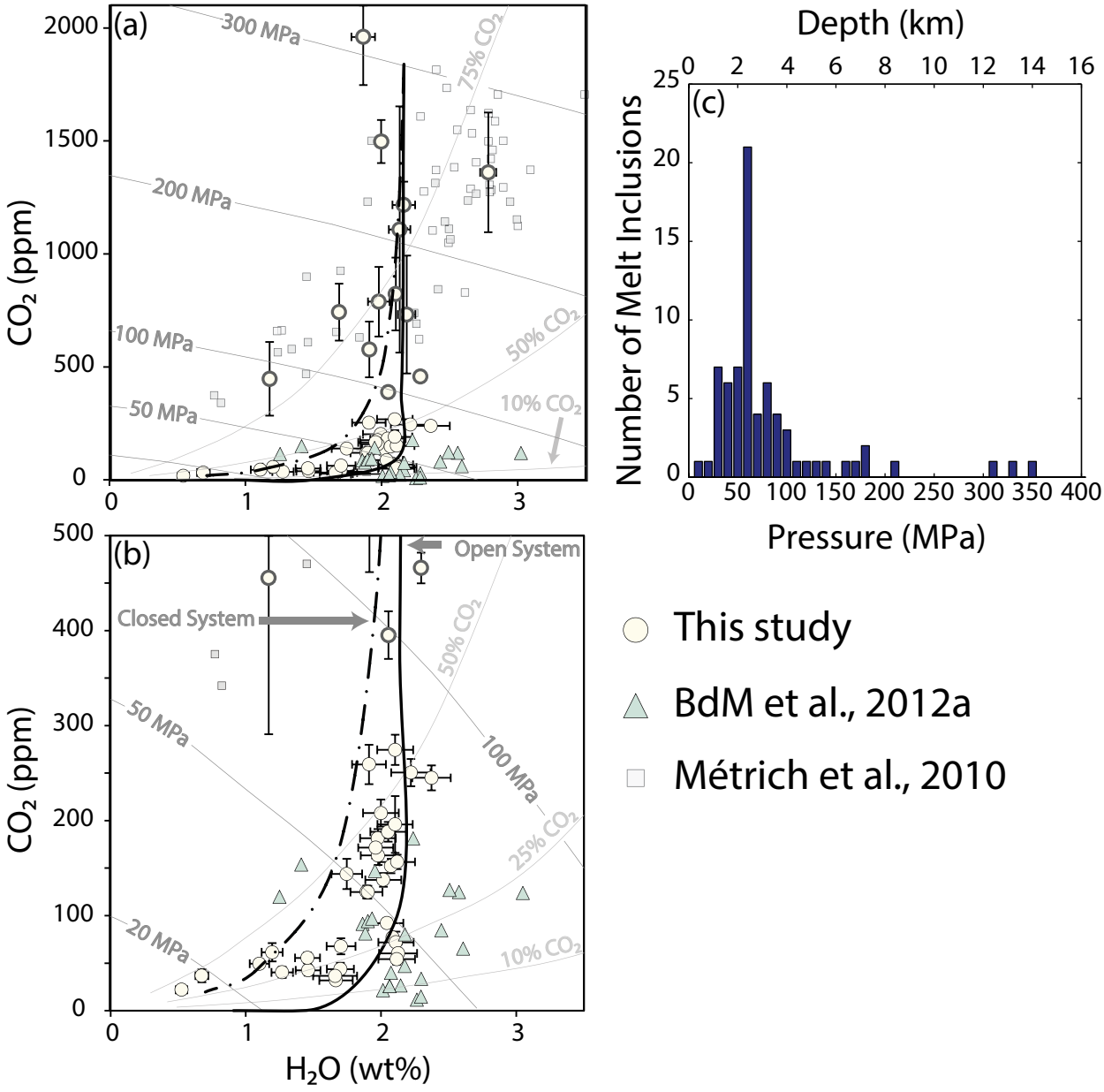

Figure 15. We used the model of Papale et al. (2006) to assess degassing style recorded by the melt inclusions. a) Plots of CO2 vs H2O from melt inclusions to show degassing behavior. Bold circles were analyzed with FTIR whereas the solid circles were analyzed with SIMS. The error bars are 2 sigma. Open (solid, black line) and closed (dash, black line) system degassing are modelled from 2000 ppm CO2, 2.15 wt% H2O. For the closed system, there is also an initial vapor phase of 1%. The dark gray lines are isobars and the light grey lines are isopleths showing the % CO2 in the vapor phase. All lines produced with Papale et al. (2006). b) Is a zoomed in version of a), note the vertical scale change. All symbols as in Figure 12. For comparison, melt inclusion volatile contents from paroxysmal eruptions at Stromboli reported in Métrich et al. (2010) are also plotted in a) and b). c) is a histogram showing the distribution of entrapment pressures for the plumbing system. Note the peak at 80 MPa.

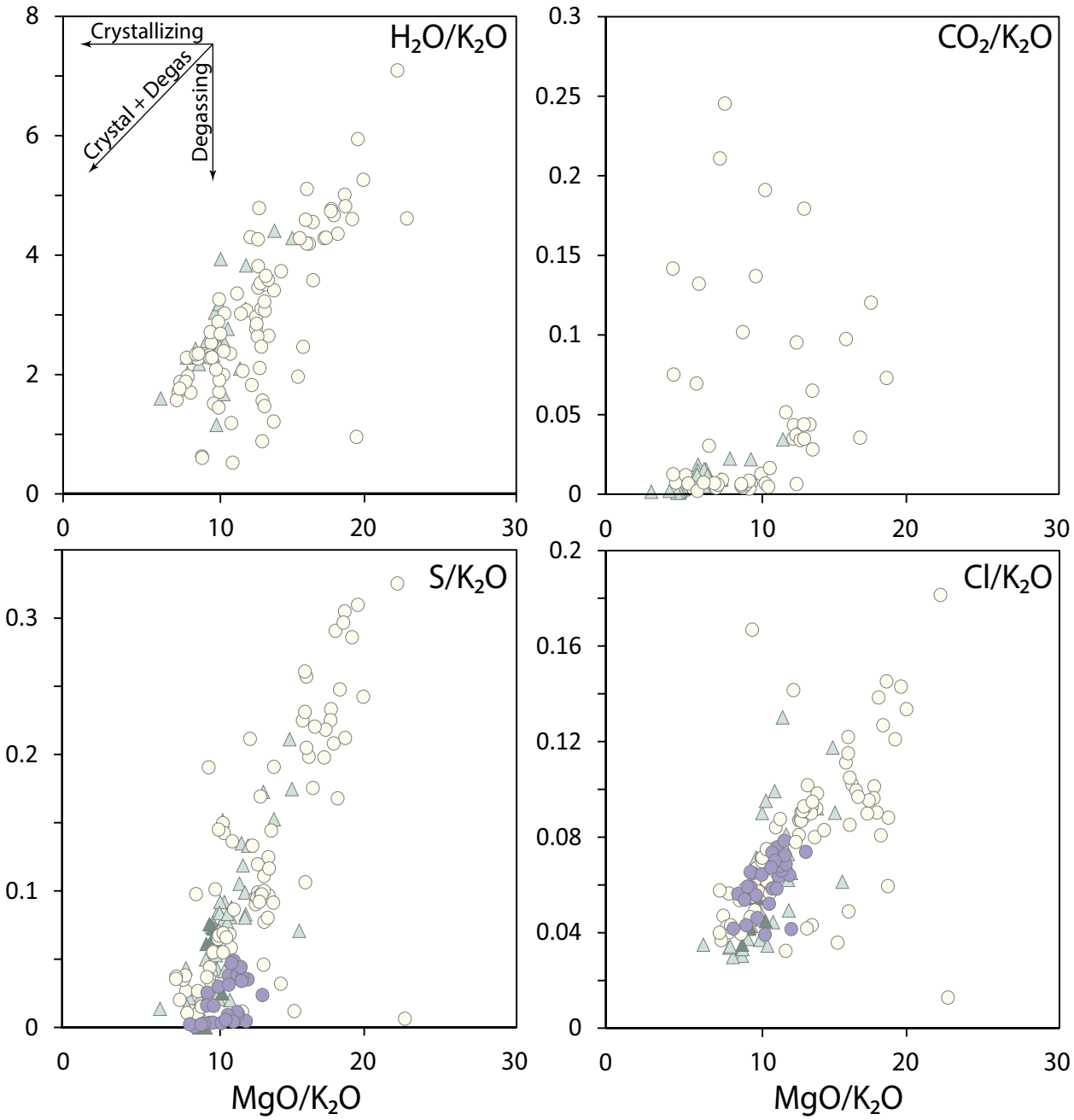

Figure 16. Volatiles ratios to K2O to show the relationship between degassing and crystallization. H2O, S, and Cl show good correlations with K2O, indicating that degassing and crystallization are coupled. CO2 shows more scatter, but at lower values (i.e. inferred shallower levels), degassing and crystallization are coupled. Matrix glass values for S and Cl provide information about degassing during the eruption. Both Cl and S in the matrix glass decrease, indicating syn-eruption degassing. Very low S values in the matrix glass suggest almost complete degassing whereas Cl did not completely degas.

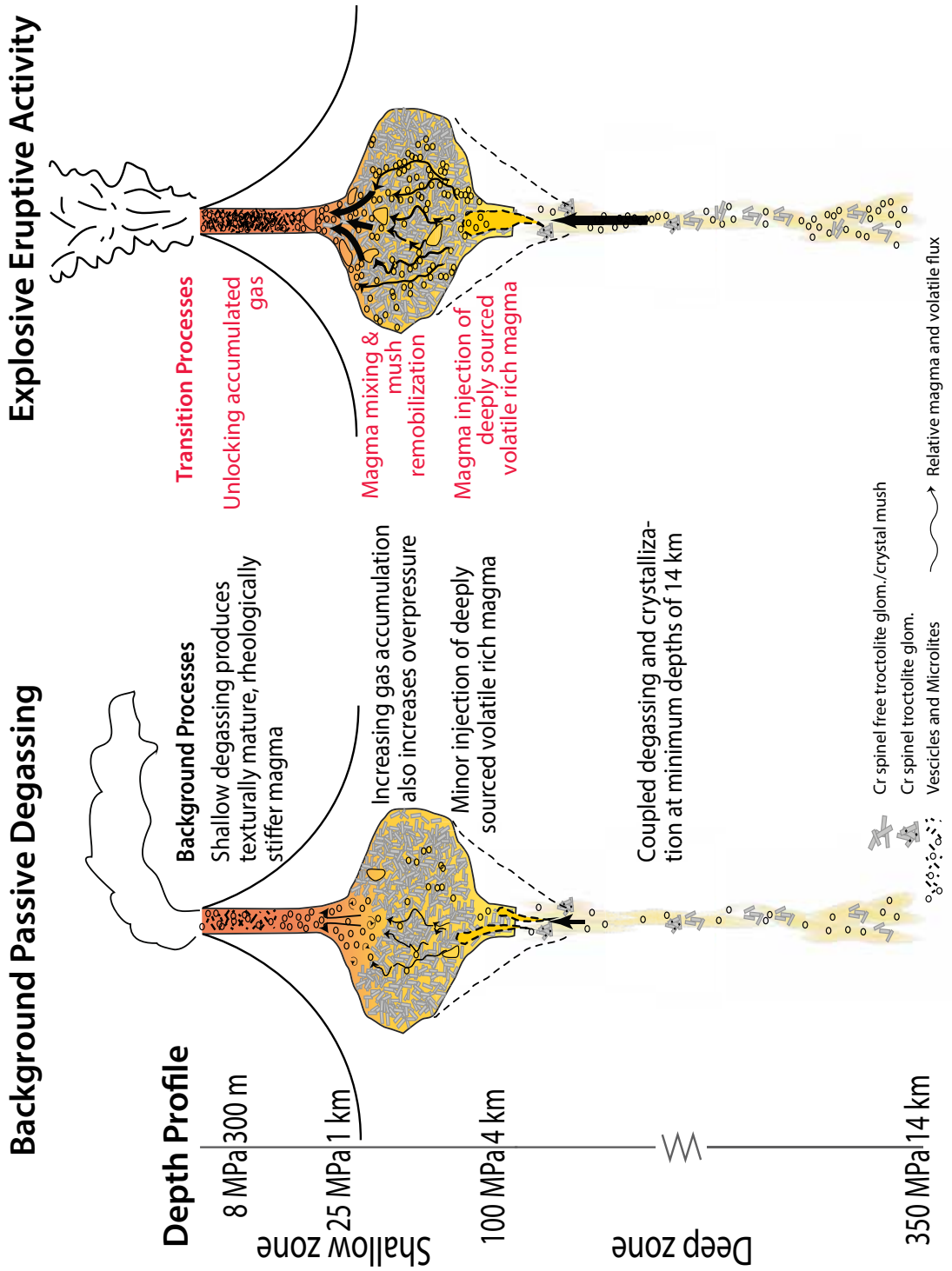

Figure 17. Schematic cartoon illustrating the plumbing system of Llaima and the key magmatic processes for the background passive degassing and transitions to the explosive eruption, respectively. Background passive degassing is characterized by continuous degassing from the summit, which results in the crystallization and rheological stiffening of the conduit magma. Minor volumes of magma are periodically injected into the crystal mush, which degasses and maintains the summit degassing. The deep plumbing system also experiences crystallization and degassing. Gas transport through the system is regulated mostly by the presence of the crystal mush, where vesicles get trapped within the interstitial spaces between crystals. Additional gas holdup may occur beneath the rheologically stiffer conduit magma. Gas may develop into larger bubbles, or more likely, foamy regions in the upper part of the crystal mush (the larger vesicles in the figure). The transition to the 2008 eruption at Llaima occurred after injection event that remobilized the crystal mush, and importantly, unlocked the accumulated gas that ascended rapidly to produce the observed explosive behavior at the summit.

Table 1. Summary table of crystalline and vesicle textures observed in the brown scoria and black lapilli scoria. For textural information on the black plate tephra, see Ruth and Calder (2014).

	Vesicles	Crystallinity (phenocrysts +groundmass)	Phenocrysts	Micro-phenocrysts	Microlites	Matrix glass	Other
Black scoria	79% convolute	50-60 vol%	4-7 vol% plg, ol	plg: normally zoned, pristine	plg: tabular and acicular, interlocking configuration	Limited	
Brown scoria	88%, round	10-15 vol%	1-2 vol% plg, ol	Rarely observed	plg: acicular, sometimes tabular	Abundant	Domains with black scoria textures

Table 2. Textural input and output for vesicle size distribution measurements. Average diameter = 2(area fraction/(π*vesicle number density))$^{1/2}$.

Sample	Total Area Measured (mm^2)	Phenocryst area (mm^2)	Total Area – Phenocryst Area	Number of vesicles measured	VND	Average diameter (mm)	SD (mm)
Brown	18.8	0.2	18.6	2315	124	0.055066	0.058757
brown	9.1	0.2	8.9	1260	142	0.044447	0.052181
1Black	13.7	0.6	13.0	2162	166	0.074175	0.155396
2Black	19.6	1.4	18.2	1935	106	0.074638	0.1865

Table 3. Textural inputs for crystal size distribution measurements. Crystal number density is the number of crystals per unit area.

Sample	Total Area (mm^2)	Total Bubbles Area (mm^2)	% Bubbles	Major axis	Intermediate axis	Minor axis	Number of crystals measured	CND
Brown	14.1374	10.41910152	73.7	2	1	1	5487	1476
Brown1	16.1369	11.8370804	73.4	2	1	1	5893	1371
BrownLL	1.5206	0.77426498	50.9	1.15	1.05	1	7485	10029
Black	6.9795	2.74364145	39.3	2	1	1	9298	2195
1Black	3.4565	1.72197592	49.8	10	1	1	8636	4979
2Black	7.511	3.7982712	50.6	2	1	1	9279	2499
Plate	2.2893	0.41159049	18	10	1	1	7917	4216
Plate3	3.7005	0.2743954	7.4	10	1	1	7332	2140

Table 4. Representative mineral analyses (olivine, plagioclase, spinel) obtained with the electron microprobe.

	BRN3-1-2010	bk2-5-1-2012	br3-1-1-2012	br4-2-2-2012	3 blk_ol_2-52	15 brn_ol_3-199	7 blk_ol_6-128	6 blk_ol_5-95
Type	Host ol	Host ol	Host ol	Host ol	Glom. ol	Glom. ol	Glom. ol	Glom. ol
SiO_2	36.41	38.74	39.67	40.21	37.67	40.59	39.24	37.67
TiO_2	nd*	0.05	0.01	0.01	nd	nd	nd	nd
Al_2O_3	nd	0.02	0.01	0.02	nd	nd	nd	nd
Cr_2O_3	0.00	0.01	0.02	0.02	0.01	0.02	0.02	0.01
FeO	30.14	21.24	18.02	14.99	19.09	17.24	16.97	16.99
MnO	0.49	0.33	0.27	0.22	0.31	0.27	0.27	0.27
MgO	33.74	39.23	42.07	44.88	40.90	40.76	42.73	46.10
NiO	0.07	0.11	0.13	0.20	0.11	0.15	0.16	0.12
CaO	0.27	0.22	0.19	0.18	0.22	0.20	0.20	0.25
Total	101.11	99.94	100.38	100.72	98.32	99.22	99.60	101.40
Si	0.98	1.00	1.01	1.00	0.99	1.03	1.00	0.95
Ti	nd	0.00	0.00	0.00	nd	nd	nd	nd
Al	nd	0.00	0.00	0.00	nd	nd	nd	nd
Cr	0.00	0.00	0.00	0.00	0.00	0.00	0.00	0.00
Fe^{2+}	0.68	0.46	0.38	0.31	0.42	0.37	0.36	0.36
Mn	0.01	0.01	0.01	0.00	0.01	0.01	0.01	0.01
Mg	1.35	1.51	1.59	1.67	1.60	1.55	1.62	1.73
Ni	0.00	0.00	0.00	0.00	0.00	0.00	0.00	0.00
Ca	0.01	0.01	0.01	0.00	0.01	0.01	0.01	0.01
∑Cation	3.02	3.00	2.99	3.00	3.01	2.97	3.00	3.05
%Fo	66.25	76.42	80.39	84.03	78.98	80.58	81.54	82.64

Table 4. Continued.

Type	13 brn_plg_3-236 Glom. plag	15 brn_plg_5-269 Glom. plag	Black-655 Scoria plag	WAQ-738 Scoria plag	WAQ-737 Scoria plag	Black-657 Scoria plag	Black-656 Scoria plag	ZRN - 732 Scoria plag
SiO_2	44.46	44.07	53.75	52.52	52.57	52.18	49.38	47.70
TiO_2	0.03	0.00	0.036	0.175	0.068	0.036	0.007	0.018
Al_2O_3	33.95	34.39	28.75	29.11	29.89	30.00	32.56	32.81
FeO	0.57	0.54	1.22	1.08	0.92	0.84	0.95	0.58
MgO	0.07	0.07	0.31	0.33	0.26	0.26	0.30	0.12
CaO	18.08	18.39	11.80	12.24	13.21	13.54	13.08	16.85
Na_2O	1.09	0.87	4.24	4.14	3.87	3.74	3.32	2.01
K_2O	0.02	0.01	0.17	0.16	0.12	0.07	0.11	0.02
Total	98.27	98.34	100.28	99.75	100.90	100.67	99.70	100.11
Si	2.09	2.08	2.43	2.40	2.37	2.36	2.26	2.19
Ti	0.00	0.00	0.00	0.01	0.00	0.00	0.00	0.00
Al	1.88	1.91	1.53	1.56	1.59	1.60	1.76	1.78
Fe^{2+}	0.02	0.02	0.05	0.04	0.03	0.03	0.04	0.02
Mg	0.00	0.01	0.02	0.02	0.02	0.02	0.02	0.01
Ca	0.91	0.93	0.57	0.60	0.64	0.66	0.64	0.83
Na	0.10	0.08	0.37	0.37	0.34	0.33	0.29	0.18
K	0.00	0.00	0.01	0.01	0.01	0.00	0.01	0.00
∑Cation	5.02	5.02	4.99	5.00	5.00	5.00	5.01	5.01
%An	90.07	92.05	59.97	61.41	64.90	66.42	68.05	82.18

Table 4. Continued

	17 Llaima5-287	18 Llaima6-294	18 Llaima7-295	19 Llaima7-296	20 Llaima8-301	21 Llaima9-304	24 Llaima12-311
Type	oxide	oxide	oxide	oxide	oxide	oxide	oxide
SiO_2	0.08	0.10	0.11	0.20	0.16	0.05	0.11
TiO_2	0.61	1.25	1.25	0.63	1.40	1.03	1.46
Al_2O_3	31.19	27.79	27.29	32.94	20.80	27.52	21.87
Cr_2O_3	23.06	22.50	22.84	22.99	27.28	23.41	25.57
FeO	29.80	36.23	36.89	29.83	39.07	35.92	39.70
MnO	0.19	0.23	0.19	0.16	0.23	0.19	0.24
MgO	14.51	12.74	12.68	14.59	10.18	12.94	10.99
CaO	0.24	0.21	0.16	0.20	0.37	0.12	0.26
Total	99.69	101.05	101.40	101.53	99.49	101.18	100.20
Si	0.00	0.00	0.00	0.00	0.00	0.01	0.00
Ti	0.03	0.03	0.03	0.03	0.07	0.01	0.03
Al	0.94	0.86	0.79	0.74	0.53	1.11	0.77
Cr	0.55	0.60	0.62	0.73	0.66	0.52	0.68
Fe^{3+**}	0.46	0.48	0.52	0.48	0.66	0.34	0.51
Fe^{2+**}	0.45	0.48	0.50	0.50	0.60	0.37	0.52
Mn	0.01	0.01	0.01	0.01	0.01	0.00	0.01
Mg	0.55	0.53	0.51	0.50	0.46	0.62	0.48
Ni	0.00	0.00	0.00	0.00	0.00	0.00	0.00
∑Cation	2.99	3.00	2.99	2.99	3.00	2.99	2.99
Cr#	28.31	30.87	32.10	37.27	35.86	26.38	34.68

*n.d. indicates not determined.

**Fe^{2+} and Fe^{3+} determined through charge balancing.

Table 5. Oxygen fugacity calculations using equation 7 from Kress and Carmichael (1991). All calculations at the given pressure and temperature.

Sample	BLK1-1-2010	blk3-MI-1-2011	blk8-MI-1-2011	brn8-MI-1-2011
SiO_2	52.04	53.09	51.68	50.93
TiO_2	1.01	1.55	0.92	1.06
Al_2O_3	15.74	12.89	16.95	16.96
FeO*	9.38	11.01	9.81	9.11
MnO	0.20	0.19	0.16	0.15
MgO	4.16	5.35	4.81	5.44
CaO	8.76	7.48	9.02	9.02
Na_2O	3.29	3.04	3.24	3.33
K_2O	0.64	1.04	0.49	0.60
P_2O_5	0.27	0.29	0.15	0.19
Sum	95.48	95.94	97.23	96.79
T (°C)	1147	1188	1131	1152
P (MPa)	50	50	50	50
$Fe^{3+}/\sum Fe$	0.15	0.15	0.15	0.15
ΔNNO	-0.72	-0.63	-0.66	-0.71
$Fe^{3+}/\sum Fe$	0.20	0.20	0.20	0.20
ΔNNO	+0.06	+0.14	+0.12	+0.07
$Fe^{3+}/\sum Fe$	0.25	0.25	0.25	0.25
ΔNNO	+0.693	+0.779	+0.75	+0.71

Table 6. Representative major element and volatile concentrations in melt inclusions. These measurements are after post entrapment correction. Uncorrected data can be found in the supplemental material. Melt inclusions labeled int were located in between the core and the rim.

Sample	br1-3-3-2012	blk11-MI-5-2011	br1-3-2-2012	BRN6-3 - 2010*	bk3-2-1-2012	bk1-2-1-2012	blk8-MI-4-2011	blk7-MI-2-2011
MI Location	int	rim	core	core	int	int	int	int
MI Size (um)	90	41	104	18	113	101	40	82
Bubble	no	no	yes	no	no	no	yes	no
% PEC	1	4	1	4	0	4	5	3
SiO_2	49.02	49.76	50.21	50.72	50.72	50.74	50.97	51.52
TiO_2	1.08	0.99	0.97	0.95	0.94	0.89	1.08	0.92
Al_2O_3	17.52	16.62	16.71	18.35	18.58	16.96	16.77	17.50
FeOt	11.34	12.29	11.34	9.19	9.45	11.30	11.17	10.05
Fe_2O_3	1.80	1.98	1.80	1.23	1.33	1.69	1.73	1.46
FeO	9.71	10.51	9.73	8.09	8.25	9.78	9.61	8.73
MnO	0.19	0.22	0.14	0.21	0.16	0.17	0.18	0.17
MgO	6.47	6.62	6.46	6.84	6.14	6.48	6.53	6.46
CaO	10.47	9.80	10.35	10.21	10.18	9.99	9.45	9.47
Na_2O	2.97	2.98	2.93	2.78	3.06	2.77	3.02	3.20
K_2O	0.55	0.38	0.50	0.42	0.48	0.38	0.48	0.40
P_2O_5	0.20	0.15	0.19	0.20	0.15	0.15	0.19	0.16
Total	100.00	100.00	100.00	100.00	100.00	100.00	100.00	100.00
mg#	0.50	0.49	0.50	0.57	0.54	0.51	0.51	0.53
Host Fo	80	79	80	83	82	80	80	81
S (ppm)	n.d.	n.d.	n.d.	n.d.	n.d.	927	1244	1153
Cl (ppm)	n.d.	n.d.	n.d.	n.d.	n.d.	511	549	488
F (ppm)	n.d.	n.d.	n.d.	n.d.	n.d.	305	0	0
H_2O (wt%)	n.d.	0.37	n.d.	n.d.	n.d.	2.01	n.d.	2.05
H_2O error	n.d.	0.14	n.d.	n.d.	n.d.	0.13	n.d.	0.02
CO_2 (ppm)	n.d.	n.d.	n.d.	n.d.	n.d.	138	n.d.	394
CO_2 error	n.d.	n.d.	n.d.	n.d.	n.d.	7	n.d.	25
Temp (°C)	1218	1180	1212	1179	1206	1173	1158	1185
Pressure (MPa)	n.d.	n.d.	n.d.	n.d.	n.d.	49	n.d.	81
Depth (km)	n.d.	n.d.	n.d.	n.d.	n.d.	2.0	n.d.	3.3

n.d. indicates not determined

Table 6. Continued.

Sample	blk9-MI-1-2011	BUL4-3-2010*	BUL4-1-2010*	br2-1-1-2012	brn5-MI-1-2011	bk2-8-1-2012	bk4-2-2-2012	bk4-1-1-2012
MI Location	rim	int	int	int	core	core	rim	core
MI Size (um)	34	16	20	30	50	158	65	184
Bubble	no	yes	yes	no	yes	no	no	no
% PEC	4	1	0	0	0	1	2	0
SiO_2	51.54	51.55	52.01	52.02	52.20	52.22	52.25	52.65
TiO_2	1.22	1.02	1.11	1.18	1.10	1.10	1.04	1.68
Al_2O_3	15.86	17.54	17.01	17.55	17.59	17.09	16.96	11.99
FeOt	11.53	10.34	10.66	9.92	10.14	9.71	9.94	15.22
Fe_2O_3	1.90	1.57	1.65	2.21	2.26	1.50	1.52	3.14
FeO	9.82	8.93	9.18	7.94	8.11	8.36	8.57	12.39
MnO	0.20	0.25	0.22	0.20	0.19	0.16	0.17	0.23
MgO	6.52	5.74	6.08	5.22	5.25	5.94	5.84	5.99
CaO	8.98	9.59	8.82	9.65	9.51	9.49	9.65	8.29
Na_2O	3.04	3.04	3.01	3.54	3.24	3.34	3.21	2.76
K_2O	0.73	0.55	0.66	0.56	0.59	0.61	0.61	0.55
P_2O_5	0.19	0.21	0.26	0.17	0.19	0.19	0.19	0.33
Total	100.00	100.00	100.00	100.22	100.23	100.00	100.00	100.00
mg#	0.50	0.50	0.50	0.48	0.48	0.52	0.51	0.41
Host Fo	80	79	79	76	77	81	80	68
S (ppm)	400	n.d.	n.d.	512	454	553	577	175
Cl (ppm)	545	n.d.	n.d.	515	597	495	532	454
F (ppm)	0	n.d.	n.d.	300	n.d.	311	324	289
H_2O (wt%)	n.d.	n.d.	2.00	0.68	n.d.	1.70	1.61	2.04
H_2O error	n.d.	n.d.	0.04	0.05	n.d.	0.10	0.10	0.12
CO_2 (ppm)	n.d.	n.d.	n.d.	37	n.d.	44	25	92
CO_2 error	n.d.	n.d.	n.d.	7	n.d.	7	2	5
Temp (°C)	1171	1193	1219	1197	1192	1196	1176	1190
Pressure (MPa)	n.d.	n.d.	n.d.	13	n.d.	31	26	73
Depth (km)	n.d.	n.d.	n.d.	0.5	n.d.	1.3	1.1	3.0

Table 6. Continued.

Sample	bk4-4-1-2012	brn6-MI-1-2011	bk3-4-3-2012	Plate1-2010*	blk9-MI-2-2011	brn4-MI-1-2011	blk5-MI-1-2011	bk2-6-1-2012
MI Location	int	core	int	core	int	int	core	int
MI Size (um)	90	93	105	33	38	106	157	102
Bubble	no	no	yes	no	yes	no	no	yes
% PEC	0	0	2	1	3	0	5	0
SiO_2	52.88	52.90	52.93	54.06	54.06	54.08	54.21	54.24
TiO_2	0.73	1.23	0.88	0.82	1.90	1.65	1.43	1.52
Al_2O_3	17.47	14.95	16.87	16.36	14.00	13.01	15.71	13.53
FeOt	9.48	14.13	9.86	10.15	11.04	13.54	10.92	12.23
Fe_2O_3	1.36	2.82	1.54	1.53	1.99	2.71	2.04	2.72
FeO	8.26	11.60	8.48	8.78	9.25	11.11	9.08	9.78
MnO	0.19	0.24	0.18	0.20	0.19	0.21	0.22	0.23
MgO	6.01	4.62	5.79	5.81	5.86	5.48	3.93	5.33
CaO	9.32	7.57	9.01	8.58	8.55	7.46	8.99	8.93
Na_2O	3.25	3.08	3.73	3.11	2.99	2.97	3.36	2.98
K_2O	0.44	0.73	0.46	0.58	0.92	0.98	0.72	0.64
P_2O_5	0.09	0.27	0.14	0.17	0.28	0.35	0.30	0.37
Total	100.00	100.00	100.00	100.00	100.00	100.00	99.99	100.28
mg#	0.53	0.37	0.51	0.51	0.49	0.42	0.39	0.44
Host Fo	81	68	80	80	79	71	72	72
S (ppm)	731	482	995	n.d.	895	104	618	n.d.
Cl (ppm)	352	412	435	n.d.	491	423	512	n.d.
F (ppm)	218	n.d.	257	n.d.	n.d.	n.d.	n.d.	n.d.
H_2O (wt%)	1.90	n.d.	1.96	1.98	n.d.	1.93	n.d.	n.d.
H_2O error	n.d.	n.d.	0.13	0.08	n.d.	0.10	n.d.	n.d.
CO_2 (ppm)	125	n.d.	171	796	n.d.	n.d.	n.d.	n.d.
CO_2 error	7	n.d.	11	155	n.d.	n.d.	n.d.	n.d.
Temp (°C)	1215	1186	1178	1197	1176	1209	1224	1213
Pressure (MPa)	45	n.d.	55	151	n.d.	n.d.	n.d.	n.d.
Depth (km)	1.8	n.d.	2.2	6.1	n.d.	n.d.	n.d.	n.d.

Table 6. Continued.

Sample	br1-2-1-2012	BLK8-1-2010*	br4-3-3-2012	br1-5-1-2012	brn14-MI-1-2011	brn12-MI-1-2011*	blk1-MI-1-2011	bk3-2-2-2012	BUL1-2010*
MI Location	core	int	rim	core	core	int	core	int	rim
MI Size (um)	131	60	111	42	92	123	236	57	60
Bubble	no	no	no	no	no	no	no	no	no
% PEC	0	5	1	0	0	0	0	2	0
SiO_2	54.31	54.38	54.47	54.92	54.93	55.03	55.05	55.15	56.04
TiO_2	1.55	1.35	1.15	1.77	1.70	1.76	1.75	0.65	1.53
Al_2O_3	12.91	16.05	16.65	13.02	13.36	12.85	13.34	16.72	15.13
FeOt	12.98	9.76	9.27	13.49	12.41	13.63	12.61	8.73	10.40
Fe_2O_3	2.50	1.54	1.53	2.85	2.42	2.93	2.56	1.30	1.81
FeO	10.73	8.38	7.90	10.93	10.23	10.99	10.31	7.55	8.78
MnO	0.22	0.16	0.17	0.20	0.26	0.24	0.24	0.17	0.23
MgO	5.77	5.77	5.19	4.63	5.07	4.56	4.79	5.62	4.51
CaO	7.82	8.05	8.12	7.42	7.81	7.18	7.50	8.43	7.60
Na_2O	3.08	3.12	4.04	3.14	3.09	3.11	3.09	3.78	3.06
K_2O	0.84	0.93	0.62	0.84	0.84	1.01	1.06	0.51	0.99
P_2O_5	0.26	0.29	0.16	0.28	0.29	0.34	0.32	0.10	0.32
Total	100.00	100.00	100.00	100.00	100.00	100.00	100.00	100.00	100.00
mg#	0.44	0.51	0.50	0.38	0.42	0.37	0.40	0.53	0.44
Host Fo	73	80	80	69	73	69	72	82	75
S (ppm)	299	n.d.	n.d.	330	258	268	215	n.d.	n.d.
Cl (ppm)	462	n.d.	n.d.	515	412	406	500	n.d.	n.d.
F (ppm)	478	n.d.	n.d.	606	n.d.	n.d.	n.d.	n.d.	n.d.
H_2O (wt%)	1.91	2.17	n.d.	2.12	1.91	2.30	2.00	n.d.	1.69
H_2O error	0.12	0.08	n.d.	0.14	0.04	0.04	0.04	n.d.	0.04
CO_2 (ppm)	259	1226	n.d.	61	584	n.d.	1508	n.d.	750
CO_2 error	21	103	n.d.	9	124	n.d.	96	n.d.	126
Temp (°C)	1225	1128	1182	1202	1201	1200	1196	1182	1175
Pressure (MPa)	108	205	n.d.	57	174	n.d.	342	n.d.	165
Depth (km)	4.4	8.4	n.d.	2.3	7.1	n.d.	13.9	n.d.	6.7

Table 7. Analytical results (range, average, and standard deviation) for melt inclusion volatiles measured with FTIR, SIMS, and EPMA.

	H_2O (wt%)	CO_2 (ppm)	S (ppm)	Cl (ppm)	F (ppm)
FTIR	0.36-2.94	394-1973			
(H_2O, n=54; CO_2, n=13)	(1.8±0.61)	(939±473)			
SIMS	0.53-2.37	22-274	92-1277	236-641	155-606
(n=32)	(1.76±0.44)	(110±77)	(639±290)	(478±86)	(322±89)
EPMA			23-1534	47-1342	
(n=47)			(699±415)	(490±183)	

Standard deviations are 2σ. *N* equals number of analyses.

Table 8. Inputs and viscosity modeling results based on different crystallinity in the scoria. Model inputs include the average whole rock chemistry with all major elements in wt%, assumed water content of 1 wt%, and the temperature from the plagioclase melt thermometer. The reported values are for both the Shaw model and the Bottinga and Weill model.

Model Inputs												
SiO_2	TiO_2	Al_2O_3	Fe_2O_3	FeO	MnO	MgO	CaO	Na_2O	K_2O	P_2O_5	H_2O	T °C
51.35	1.02	18.25	2.76	8.94	0.16	5.75	9.89	3.09	0.57	0.19	1.0	1150

	8 MPa		15 MPa		30 MPa	
	Shaw	B&W	Shaw	B&W	Shaw	B&W
Black Scoria – 50% crystallinity	$5.64x10^4$	$2.80x10^4$	$2.29x10^4$	$2.35x10^4$	$2.29x10^4$	$2.35x10^4$
Brown Scoria – 10% crystallinity	$1.33x10^2$	$1.59\ x10^2$	$4.45x10^1$	$5.40x10^1$	$4.45x10^1$	$5.40x10^1$

Model inputs include the average whole rock chemistry with all major elements in wt%, assumed water content of 1 wt%, and the temperature from the plagioclase melt thermometer. The reported values are for both the Shaw (1972) model and the Bottinga and Weill (1972) model.